A Novel Dimension-Reduced Space-Time Adaptive Processing Algorithm for Spaceborne Multichannel Surveillance Radar Systems Based on Spatial-Temporal 2-D Sliding Window

Penghui Huang, *Member, IEEE*, Zihao Zou, Xiang-Gen Xia, *Fellow, IEEE*, Xingzhao Liu, *Member, IEEE*, and Guisheng Liao, *Senior Member, IEEE*

Abstract—When an early warning radar installed in a spaceborne platform works in a down-looking mode to detect a low-altitude flying target, the severely broadened main-lobe clutter cannot be ignored, which will cause the deterioration of moving target detection capability. To deal with this problem, a space-time adaptive processing (STAP) technique is proposed for effective clutter suppression based on the spatial-temporal 2-D joint filtering. However, the full-dimensional optimal STAP encounters the challenges of high computational complexity and large training sample requirement. Therefore, the dimension-reduced STAP technique becomes necessary. This paper proposes a novel dimension-reduced STAP algorithm based on spatial-temporal 2-D sliding window processing. Firstly, several sets of spatial-temporal data are obtained by using spatial-temporal 2-D sliding window. Then, for each set of data, the 2-D discrete Fourier transform is performed to transform the echo data into angle-Doppler domain. Finally, the jointly adaptive processing is performed to realize the clutter suppression. Compared with the conventional STAP algorithms, the improvements of this method over the existing methods are: 1) the proposed method requires fewer training samples due to the 2-D localization processing; and 2) the proposed method can obtain the better clutter suppression performance with a lower computational complexity. The feasibility and effectiveness of the proposed algorithm are verified by both simulated and real-measured multichannel surveillance radar data.

Index Terms—Space-time adaptive processing (STAP), dimension-reduced STAP, clutter suppression, early warning surveillance radar.

I. INTRODUCTION

Early warning surveillance radars possess the capabilities of wide range, high revisit frequency, and all-weather moving target detection, localization, tracking, and identification. They have attracted much attention in recent decades [1], [2]. The traditional ground-based and shipborne monitoring radars are inevitably limited by the earth curvature and the terrain occlusion, exhibiting the limited detection range. Compared to long-range surveillance radar installed on a static or slow-moving platform, spaceborne radar systems have higher maneuverability and wider detection range in virtue of the advantage of platform height, and have been widely applied in military reconnaissance, traffic monitoring, and meteorological monitoring [3]-[6]. However, when a warning radar installed on a spaceborne platform works in a down-looking mode, the severe broadening of main-lobe clutter under the dual-modulations of transmitting and receiving antenna patterns will occur due to the Doppler center shifts of different ground scatter points relative to the high-speed platform motion. Therefore, robust clutter suppression processing is a key procedure in moving target detection.

For the conventional ground-based and ship-borne radar systems, the received clutter returns are mainly concentrated in the zero-frequency region. Therefore, according to Doppler difference between a moving target and clutter signal, the clutter cancellation can be effectively achieved by using the pulse cancellation techniques in a single-channel radar configuration [1]. In addition, the Doppler filter bank and adaptive moving target detection (AMTD) technique can further improve the clutter suppression performance in complex clutter environment [7]. However, for the spaceborne radars, the high-speed platform motion will cause the Doppler spectrums of different clutter components severely broadening, significantly decreasing the moving target output signal-to-clutter-plus-noise ratio (SCNR), especially for a slow-moving target [8], [9]. In this case, it is difficult to suppress the broadened clutter by only exploiting the temporal information [10]. To address this issue, the space-time adaptive processing (STAP) technique has been developed, which utilizes the joint temporal-spatial information to achieve effective clutter suppression based on 2-D adaptive filter processing [11]. However, the full-dimensional optimal STAP suffers from the challenges of high computational complexity and huge requirement of independent and identically distributed (i.i.d.) training samples, which may be unrealistic in practical applications, especially in a relatively inhomogeneous scene [12]-[15]. Therefore, in order to reduce the computational complexity and requirement of a large number of i.i.d. samples, dimension-reduced STAP and rank-reduced STAP are developed in the last decades [16], [17].

Rank-reduced STAP adaptively constructs the spatial-temporal filter by exploiting the echo signal property. Klemm [18] has concluded that the clutter rank is approximately the sum of the numbers of transmitted pulses and spatial channels. In addition, to suppress the clutter effectively, the required degree of freedom of STAP should only be a little higher than the clutter rank, and thus the reduction of effective training sample demand by using the rank-reduced STAP techniques becomes possible. Haimovich [19] has proposed an eigencanceler based on eigendecomposition, where the clutter covariance matrix is reconstructed by selecting the eigenvectors corresponding to large eigenvalues. Goldstein *et al.* [20], [21] have proposed the cross-spectral metric (CSM) method to realize the clutter covariance matrix reconstruction based on the cross-spectral value criterion. To further reduce the computational complexity, the multistage Wiener filter (MWF) approach is proposed in [22] by decomposing the Wiener filtering process. However, the performance of rank-reduced STAP algorithms usually depends on the degree of freedom of clutter, which is difficult to be accurately estimated in the case of some nonideal system errors, restricting their applications in the practical engineering [16].

Different from the rank-reduced STAP algorithms, the dimension-reduced STAP algorithms decrease the system dimension through some kinds of linear transformations, which can effectively reduce the computational complexity and training sample demand in the transform domain [23]. Typical dimension-reduced STAP algorithms can be mainly divided into two kinds: time-space cascaded adaptive processing algorithms and joint dimension-reduced adaptive processing algorithms.

The time-space cascaded adaptive processing algorithms realize the dimension reduction in the time domain by temporal filtering and then implement the adaptive processing in spatial domain. A typical algorithm is to apply the Doppler filtering to decrease the clutter degree of freedom, and then the spatial adaptive processing is implemented to enhance the target output SCNR [24], [25]; however, due to the lack of auxiliary channels, it may exhibit a poor clutter suppression performance in the main-lobe clutter region. To solve this problem, DiPietro [25] has proposed the extended factored approach (EFA) to improve the clutter suppression performance by jointly using adjacent Doppler channels as auxiliary channels. Brennan *et al.* [26] have proposed the filter-then-adapt (F$A) algorithm to provide additional degrees of freedom via adding delayed taps, improving the subsequent clutter suppression performance. To further decrease the computing source consuming, Brown *et al.* [27] have proposed the $\Sigma\Delta$-STAP by utilizing only the sum and difference channels; however, its low spatial degree of freedom is obtained at the sacrifice of the clutter suppression performance.

Joint dimension-reduced adaptive processing algorithms transform the radar echo data in the space-time domain into the angle-Doppler domain through 2-D discrete Fourier transform (DFT), realizing the dimension reduction both in time domain and space domain. The auxiliary channel receiver (ACR) technique has been proposed by Klemm [28], which selects the auxiliary channels along the clutter ridge in the space-time spectrum. However, this method requires the precise system

parameters as a priori information. In addition, the clutter suppression performance depends on the number and selected positions of auxiliary channels, which may be easily influenced by the radar system errors. Wang *et al.* [29] have proposed the joint domain localized (JDL) algorithm to improve the clutter suppression performance via selecting the auxiliary channels around the target channel in the form of a rectangular window. To further improve the computational efficiency, the space-time multiple-beam (STMB) algorithm has been proposed by Wang *et al.* [30], [31], which effectively reduces the system dimension by selecting the auxiliary channels with a cross shape.

Motivated by the previous works, a novel dimension-reduced STAP algorithm is proposed in this paper. In the proposed algorithm, the spatial-temporal 2-D sliding window is applied to obtain multiple spatial-temporal echo data sets; then the echo data are transformed into the angle-Doppler domain by using 2-D DFT; finally, the localized adaptive processing is performed to enhance the target output SCNR. Compared with the full-dimensional optimal STAP, the proposed algorithm greatly reduces the computational load in real-time processing and the difficulty in obtaining enough i.i.d. training samples. Compared with the conventional time-space cascaded adaptive processing algorithms and the rank-reduced STAP algorithms, the proposed algorithm requires lower system dimension and fewer training samples while exhibiting good clutter suppression performance. Compared with the conventional joint dimension-reduced adaptive processing algorithms, the proposed algorithm obtains a better clutter suppression performance while maintaining a relatively low computational complexity. Both simulated and real-measured multi-channel radar data are utilized to illustrate the effectiveness of the proposed algorithm.

The rest of this paper is organized as follows. In Section II, the detailed signal model for a multi-channel spaceborne early warning radar (SEWR) system is established. Section III introduces the proposed clutter suppression algorithm and gives analysis including the choice of sliding window and the computational complexity. Section IV presents some simulated and real-measured radar data processing results and gives discussions and comparisons to validate the proposed algorithm. Finally, some conclusions are drawn in Section V.

II. RECEIVING SIGNAL MODEL

Assume that the side-looking SEWR system has N spatial channels uniformly distributed along the azimuth dimension, as shown in Fig. 1, where an arbitrary ground scatter $P_{r,i}$ is considered in an *O-XYZ* Cartesian coordinate, with *X-axis* denoting the radar motion trajectory with an along-track velocity of v_p, *Y-axis* corresponding to the range coordinate, and *Z-axis* satisfying the left-hand coordinate rule with the platform height denoted by H. In Fig. 1, d_T denotes the distance between the transmitting channel center and the first receiving channel center, and $d_n = (n-1)d$, ($n = 2,3,\cdots,N$), corresponds to the physical baseline between the n th receiving channel center and the first receiving channel center, with d

being the physical distance between two adjacent channels. For a random ground scatter point $P_{r,i}$, the angles φ_r and θ_i denote, respectively, the elevation angle and azimuth angle with respect to the radar antenna array, and $R_0 = H/\cos(\varphi_r)$ refers to the initial slant range.
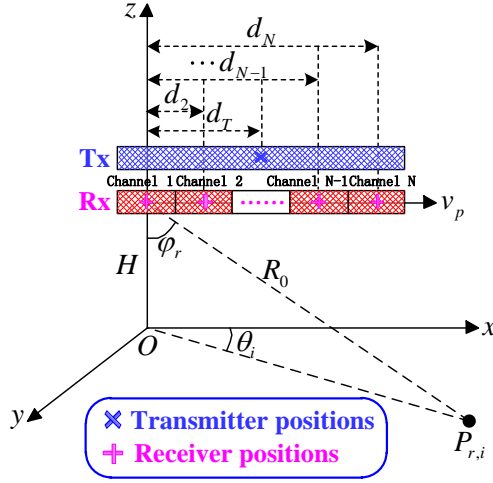

Fig. 1. 3-D geometric relationship between the spaceborne multi-channel radar platform and a ground static scatter point.

For a SEWR system, the whole antenna aperture will usually be adopted to transmit the radar signal in order to increase the radar power-aperture product [32]-[35], thus improving the weak moving target detection performance. It is different from the typical multi-channel high-resolution wide-swath (HRWS) synthetic aperture radar (SAR) imaging system [36]-[39] or SAR ground moving target indication (SAR-GMTI) system [40]-[44]. Then according to Fig. 1, the two-way slant range of $P_{r,i}$ with respect to the nth receiving channel, denoted by $R_{n,r,i}(t_m)$, is given by

$$R_{n,r,i}(t_m) = \frac{1}{2}\sqrt{\begin{array}{c}(R_0 \sin\varphi_r \cos\theta_i - v_p t_m - d_T)^2 \\ + (R_0 \sin\varphi_r \sin\theta_i)^2 + (R_0 \cos\varphi_r)^2\end{array}}$$
$$+ \frac{1}{2}\sqrt{\begin{array}{c}(R_0 \sin\varphi_r \cos\theta_i - v_p t_m - d_n)^2 \\ + (R_0 \sin\varphi_r \sin\theta_i)^2 + (R_0 \cos\varphi_r)^2\end{array}} \quad (1)$$

where t_m denotes the azimuth slow-time variable. By using the second-order Taylor series expansion, $R_{n,r,i}(t_m)$ in (1) can be approximately expressed as

$$R_{n,r,i}(t_m) \approx R_0 - \sin\varphi_r \cos\theta_i v_p t_m - \frac{\sin\varphi_r \cos\theta_i (d_T + d_n)}{2}$$
$$+ \frac{(v_p t_m + d_T)^2}{4R_0} + \frac{(v_p t_m + d_n)^2}{4R_0} \quad (2)$$

Suppose that a linear frequency modulated (LFM) signal is adopted as the baseband waveform, i.e.,

$$p(t) = rect\left(\frac{t}{T_p}\right)\exp(j\pi\mu t^2)\exp(j2\pi f_c t) \quad (3)$$

where $rect(\chi)$ is a rectangle window and equals to 1 for $|\chi| \leq 0.5$, and 0, otherwise. The other symbols t, T_p, μ, and f_c denote the fast-time variable, pulse duration, chirp rate, and carrier frequency of transmitting radar waveform, respectively.

Assuming that the radar returns of the range ring with range r on the ground are composed of N_D clutter patches with different Doppler centers. Then, after applying the range compression, the received baseband signal with respect to the nth receiving channel can be noted as

$$s_{rn}(r, d_n, t_m) = \sum_{i=1}^{N_D} A_{r,i} \omega_{r,i} \, \text{sinc}\left\{\frac{2B}{c}(r - R_0)\right\}$$
$$\times \exp\left\{-\frac{j4\pi}{\lambda}\left[\begin{array}{c} R_0 - \sin\varphi_r \cos\theta_i v_p t_m \\ -\dfrac{\sin\varphi_r \cos\theta_i (d_T + d_n)}{2} \\ +\dfrac{(v_p t_m + d_T)^2}{4R_0} + \dfrac{(v_p t_m + d_n)^2}{4R_0} \end{array}\right]\right\} \quad (4)$$

where B denotes the transmitting signal bandwidth, c refers to the speed of light, λ corresponds to the signal wavelength, and $\omega_{r,i}$ is the synthetic transmitting-receiving two-way antenna pattern related to the i th clutter patch, where the receiving azimuth pattern exhibits the large main-lobe width because of the spatial channel division. Based on the radar equation [45], the range-compressed signal amplitude, denoted by $A_{r,i}$, is

$$A_{r,i} = \sqrt{\frac{P_{av} G_T G_{R,n} \sigma_{r,i}^0 \rho_{gr} \rho_a \lambda^2 B T_{PRT}}{(4\pi)^3 R_{r,i}^4 L_s}} \quad (5)$$

where P_{av} denotes the transmitting average power, G_T denotes the transmitting antenna gain, $G_{R,n}$ is the receiving antenna gain of the nth spatial sub-channel, $\sigma_{r,i}^0$ corresponds to the backscatter coefficient of the i th clutter patch, $\rho_{gr} = c/2B\cos\delta_r$ denotes the range resolution projected along the ground (δ_r refers to the grazing angle), ρ_a denotes the azimuth resolution, T_{PRT} is the pulse repetition time (PRT), and L_s is the radar system loss, which is the sum of some energy loss terms, such as transmitting link loss, atmospheric propagation loss, ionospheric loss, sampling loss, etc. It should be noted that, different from the signal-to-noise ratio (SNR) of a moving target, the clutter power after range-azimuth compression has no relationship with the integration time because the short observation time will lead to the coarse azimuth resolution.

In practice, due to the coverage rate restriction in a wide searching mode, the beam dwell time of a SEWR system is usually provided as 10~50 ms level [32]-[35], [46]; then clutter range migration can be ignored during the relatively short observation time, and the last two terms in (4) can be approximately compensated by using the known radar

system parameters, with the chirp-compensated signal given by

$$s_{rn}(r,d_n,t_m) = \sum_{i=1}^{N_D} A_{r,i}\omega_{r,i} \operatorname{sinc}\left[\frac{2B}{c}(r-R_0)\right]$$
$$\times \exp\left\{-\frac{j4\pi}{\lambda}\left[\begin{array}{c} R_0 - \sin\varphi_r\cos\theta_i v_p t_m \\ -\dfrac{\sin\varphi_r\cos\theta_i(d_T+d_n)}{2}\end{array}\right]\right\} \quad (6)$$

Obviously, it can be observed from (6) that the temporal and spatial vectors of scatter $P_{r,i}$ are, respectively, expressed as

$$a_{t,r,i} = \exp\left(j2\pi T_{PRT}\cdot f_{a,r,i}\cdot[0,1,\cdots,K-1]^T\right) \quad (7)$$

$$a_{s,r,i} = \exp\left(j2\pi\cdot f_{s,r,i}\cdot d\cdot[0,1,\cdots,N-1]^T\right) \quad (8)$$

where "T" denotes the transpose operation, K is the pulse number, $f_{a,r,i} = \dfrac{2v_p}{\lambda}\sin\varphi_r\cos\theta_i$ represents the Doppler frequency of this scatter, and $f_{s,r,i} = \dfrac{\sin\varphi_r\cos\theta_i}{\lambda}$ corresponds to the spatial frequency.

Based on (7) and (8), the clutter temporal-spatial vector can be written as

$$a_{t-s,r,i} = a_{t,r,i}\otimes a_{s,r,i} \quad (9)$$
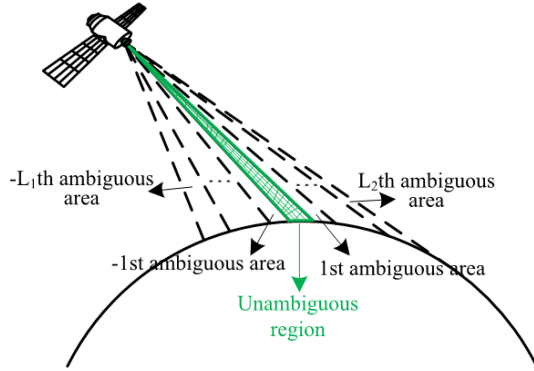
where "$\otimes$" denotes the Kronecker product.

Fig. 2. Sketch map of range ambiguity.

In addition, in order to provide the large-scale area of clean zone with the MTI mode, especially for the air moving target detection mode, the pulse repetition frequency (PRF) of transmitting radar signal is relatively high in order to enlarge the clean zone and avoid the repetitive target detection blind. Then, the range ambiguity may easily appear when the main-lobe beam of SEWR points to the far distance.

At this time, the clutter returns in a given range bin are composed of multiple range ambiguity components, and s_{rn} in

(6) should be modified as

$$s_{rn}(r,d_n,t_m) = \sum_{l=-L_1}^{L_2}\sum_{i=1}^{N_D} A_{l,r,i}\omega_{l,r,i} \operatorname{sinc}\left[\frac{2B}{c}(r-R_0)\right]$$
$$\times \exp\left\{-\frac{j4\pi}{\lambda}\left[\begin{array}{c} R_0 + \dfrac{lcT_{PRT}}{2} - \sin\varphi_{l,r}\cos\theta_{l,i}v_p t_m \\ -\dfrac{\sin\varphi_{l,r}\cos\theta_{l,i}(d_T+d_n)}{2}\end{array}\right]\right\} \quad (10)$$

where $A_{l,r,i}$, $\omega_{l,r,i}$, $\varphi_{l,r}$, and $\theta_{l,i}$ denote, respectively, the signal amplitude in the range-compressed domain, synthetic transmitting-receiving antenna pattern, elevation angle, and azimuth angle of the lth range ambiguity component, as shown in Fig. 2. In addition, the Doppler center ambiguity is considered in (10) because Doppler center frequencies of different clutter patches with different cone angles have been automatically folded into the baseband frequency of $-PRF/2 \sim PRF/2$.

After performing the Fourier transform on (10) with respect to t_m, one has

$$S_{rn}(r,d_n,f_a) = \mathscr{F}_{t_m}\left[s_{rn}(r,d_n,t_m)\right]$$
$$= \sum_{l=-L_1}^{L_2}\sum_{i=1}^{N_D} G_{azi}\cdot A_{l,r,i}\cdot\omega_{l,r,i} \operatorname{sinc}\left[\frac{2B}{c}(r-R_0)\right]$$
$$\times \operatorname{sinc}\left[KT_{PRT}\left(f_a - \frac{2v_p}{\lambda}\sin\varphi_{l,r}\cos\theta_{l,i}\right)\right] \quad (11)$$
$$\times \exp\left\{-\frac{j4\pi}{\lambda}\left[R_0 + \frac{lcT_{PRT}}{2} - \frac{\sin\varphi_{l,r}\cos\theta_{l,i}(d_T+d_n)}{2}\right]\right\}$$

where $\mathscr{F}_{t_m}$ denotes the azimuth Fourier transform operation, G_{azi} is the azimuth compression gain, and f_a corresponds to the Doppler frequency. It can be clearly seen from (11) that Doppler localization operation has significantly decreased the clutter's degree of freedom, and Doppler frequency f_a keeps one-to-one correspondence with the spatial cone angle, which is beneficial to the subsequent clutter suppression. In addition, the large azimuth antenna size is usually present in a SEWR system in order to improve the minimum detectable velocity (MDV) performance of an air moving target, and then relative to range ambiguity, Doppler center ambiguity influences corresponding to the ground scatters with the large spatial cone angles can be ignored due to the azimuth deeply weighting.

For the same reason, after performing the Fourier transform along spatial domain, the clutter signal in the angle-Doppler domain is given in (12)

$$S_{rn}(r,f_s,f_a) = \mathscr{F}_{d_n}\left[S_{rn}(r,d_n,f_a)\right]$$
$$= \sum_{l=-L_1}^{L_2}\sum_{i=1}^{N_D} G_{azi}\cdot G_{spat}\cdot A_{l,r,i}\cdot\omega_{l,r,i} \exp\left[-\frac{j4\pi}{\lambda}\left(R_0 + \frac{lcT_{PRT}}{2} - \frac{\sin\varphi_{l,r}\cos\theta_{l,i}d_T}{2}\right)\right]$$
$$\times \operatorname{sinc}\left[\frac{2B}{c}(r-R_0)\right]\operatorname{sinc}\left[KT_{PRT}\cdot\left(f_a - \frac{2v_p}{\lambda}\sin\varphi_{l,r}\cos\theta_{l,i}\right)\right]\operatorname{sinc}\left[Nd\cdot\left(f_s - \frac{\sin\varphi_{l,r}\cos\theta_{l,i}}{\lambda}\right)\right] \quad (12)$$

where $\mathscr{T}_{d_n}$ denotes the Fourier transform operation with respect to d_n and f_s denotes the spatial frequency, and G_{spat} represents the compression gain along spatial dimension. Clearly, from (12), one can see that, the clutter components will be distributed as an oblique trajectory in the angle-Doppler plane, where the more number of transmitting pulses and spatial channels, the more concentrated the clutter distribution is. In addition, for a moving target with a fixed Doppler and spatial angle, it can be represented as a point in $f_s - f_a$ plane, and this property provides the solution to filter the troubled clutter based on the 2-D dimension-reduced processing.

III. PROPOSED ALGORITHM DESCRIPTION

Due to the high-speed motion of a spaceborne platform, the broadened clutter will severely mask the moving targets, especially for slow-speed and weak targets. In addition, due to the wide-scan requirements with respect to the wide-scale scene of interest, the real-time processing in a SEWR system becomes necessary; thus, the effective and efficient clutter suppression technique is the key factor to accomplish the moving target detection and tracking in a SEWR system. In the following, let us first briefly introduce the traditional clutter suppression algorithms in a multi-channel radar configuration.

A. Traditional STAP Algorithm

1) Optimal STAP

By exploiting the 2-D temporal and spatial coupling property of clutter signal, the full-dimensional optimal STAP can effectively suppress the main-lobe clutter components based on the 2-D adaptive filtering processing with the retention of moving target signal, i.e.,

$$\begin{cases} \min w_{opt}^H R_{cn} w_{opt} \\ \text{s.t.} \ w_{opt}^H a_{target} = 1 \end{cases} \tag{13}$$

where "H" denotes the conjugate transpose operation, w_{opt} denotes the clutter suppression weight vector, R_{cn} is the covariance matrix constructed by clutter and noise components, which can be obtained based on the i.i.d. samples along range dimension. a_{target} is the target temporal-spatial steering vector with the form of

$$\begin{aligned} a_{target} = &\exp\left(j2\pi T_{PRT} \cdot f_{a,target} \cdot [0,1,\cdots,K-1]^T \right) \\ &\otimes \exp\left(j2\pi d \cdot f_{s,target} \cdot [0,1,\cdots,N-1]^T \right) \end{aligned} \tag{14}$$

where $f_{a,target}$ and $f_{s,target}$ denote the Doppler frequency and the spatial frequency of this moving target, respectively. Usually, for a SEWR system, $f_{s,target}$ can be preset according to the elevation and azimuth angles of radar beam center position. It is because that the observed target with weak radar reflectivity can be effectively captured by the radar main-lobe in an early warning radar system with the large antenna aperture, which is different from the spatial mismatch processing in a multi-channel SAR-GMTI system.

By using the Lagrange multiplier method, the optimal clutter suppression weight vector in (13), also referred to the Capon weight estimation, can be calculated as

$$w_{opt} = \frac{R_{cn}^{-1} a_{target}}{a_{target}^H R_{cn}^{-1} a_{target}} \tag{15}$$

Considering that the size of clutter covariance matrix in (13) and (15) is $NK \times NK$, the computational complexity of the full-dimensional optimal STAP will rapidly increase with the increase of pulse number and spatial channel number, which is impracticable in engineering applications due to the strict requirements of real-time processing in a SEWR system. Additionally, the large clutter degree of freedom indicates that more i.i.d. training samples are required in order to realize the accurate estimation of full-dimensional covariance matrix, which may not be easily achieved because the ground clutter patch within a wide main-lobe beam footprint may exhibit inhomogeneity [29], [31]. Therefore, the dimension-reduced STAP techniques are crucial to the practical engineering applications in a multi-channel SEWR system.

2) Filter-then-Adapt Algorithm

The filter-then-adapt algorithm in [26] is a typical dimension-reduced STAP algorithm, which effectively decreases the clutter degree of freedom by implementing the clutter Doppler localization operation. To improve the clutter suppression performance, the time-domain degree of freedom is added via the pulse delay operation, and thus multiple sets of temporal-spatial echoes can be obtained. After Doppler localization processing, the clutter suppression can be finally accomplished via the joint adaptive processing in the post-Doppler domain, as shown in Fig. 3. In addition, the influence of spectrum leakage caused by DFT is mitigated due to the fact that the signal components with different Doppler frequencies are differentiated when the time-domain sliding window is applied, further improving the clutter suppression performance.
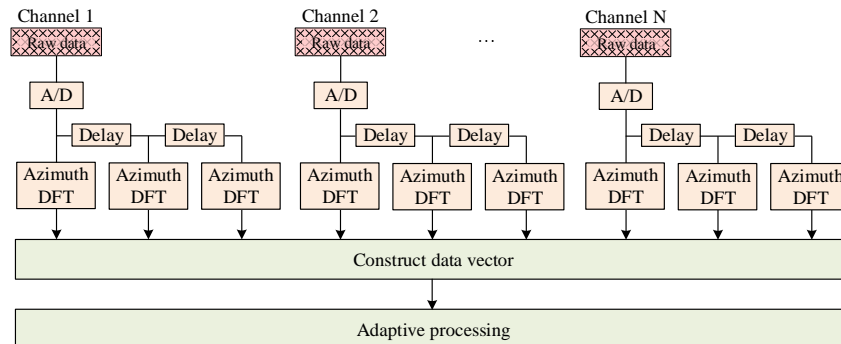

Fig. 3. Processing architecture of F$A algorithm.

Assuming that the size of the time-domain window sliding is 3, and then the size of clutter covariance matrix reduces into $3N \times 3N$, in contrast to $NK \times NK$ by using the full-dimensional STAP technique; thus its computational complexity is considerably decreased and the requirement of i.i.d. samples is dropped to $6N$. Although the time-domain degree of freedom is effectively added without increasing the integration time, the computational burden is still relatively high, especially for a large antenna array with more azimuth spatial channels [46], which may be detrimental for the real-time processing in a warning surveillance radar system with high requirement of coverage rate.

B. Proposed Algorithm

As aforementioned, the joint dimension-reduced adaptive processing algorithms achieve low computational complexity via 2-D angle-Doppler localization processing. However, after performing the 2-D DFT, the clutter components will be broadened in the angle-Doppler domain due to the signal truncation as shown in (12), leading to the spectrum leakage. Obviously, the side-lobe signal leakage from the other clutter regions will increase the degree of freedom of the current clutter component, causing the clutter suppression performance degradation. It should be noted that the 2-D weighted DFT is difficult to achieve ideal performance due to the fact that the

weighted DFT will cause the main-lobe broadening, especially for the spatial angle domain because the number of spatial receiving channels is usually less than the number of transmitting pulses. To solve this problem, the sliding window can be utilized to differentiate the components with different Doppler and spatial frequencies, benefitting to the subsequent adaptive clutter filtering.

In the following, the proposed algorithm is introduced, which extends the time-domain sliding window to the spatial-temporal 2-D sliding window, and transforms the range-compressed data into the angle-Doppler domain. Suppose that the spatial-temporal echo data contains N spatial receiving channels and K temporal pulses, and the data corresponding to the r th range ring, the n th receiving channel, and the k th pulse is denoted as $x_{r,n,k}$. Suppose that the times of space-domain window slide and time-domain window slide are P and Q, respectively. Therefore, the spatial-temporal data matrix corresponding to the p th space-domain sliding window ($1 \le p \le P$) and the q th time-domain sliding window ($1 \le q \le Q$) is composed of the data in the p th to $(N-P+p)$ th receiving channels and the q th to $(K-Q+q)$ th pulses, as shown in Fig. 4.

$$
\begin{bmatrix}
x_{r,1,1} & x_{r,1,2} & & \cdots & \cdots & & x_{r,1,K} \\
x_{r,2,1} & x_{r,2,2} & & \cdots & \cdots & & x_{r,2,K} \\
& & \ddots & & & & \\
\vdots & \vdots & & \begin{array}{ccc} x_{r,p,q} & x_{r,p,q+1} & \cdots & x_{r,p,K-Q+q} \\ x_{r,p+1,q} & x_{r,p+1,q+1} & \cdots & x_{r,p+1,K-Q+q} \\ \vdots & \vdots & \ddots & \vdots \\ x_{r,N-P+p,q} & x_{r,N-P+p,q+1} & \cdots & x_{r,N-P+p,K-Q+q} \end{array} & & \vdots \\
& & & & & \ddots & \\
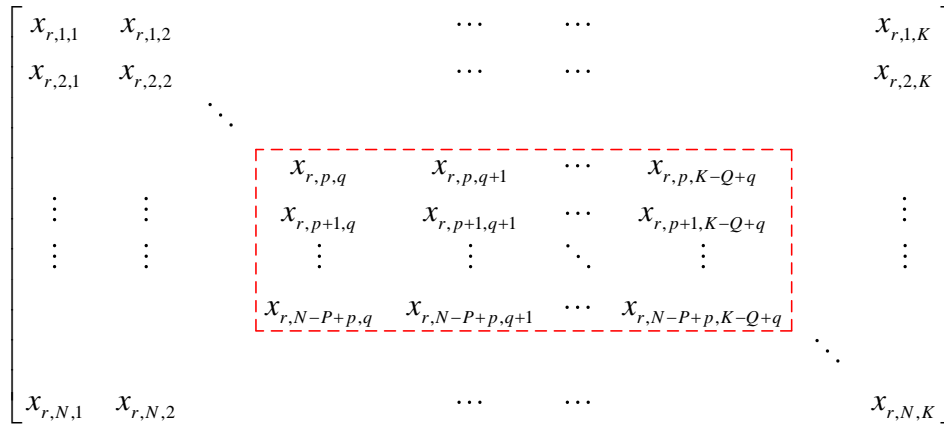x_{r,N,1} & x_{r,N,2} & & \cdots & \cdots & & x_{r,N,K}
\end{bmatrix}
$$

Fig. 4. Sketch map of spatial-temporal 2-D sliding window.

The data matrix corresponding to the p th space-domain sliding window and the q th time-domain sliding window can be expressed as

$$
X_{r,p,q} = \begin{bmatrix}
x_{r,p,q} & x_{r,p,q+1} & \cdots & x_{r,p,K-Q+q} \\
x_{r,p+1,q} & x_{r,p+1,q+1} & \cdots & x_{r,p+1,K-Q+q} \\
\vdots & \vdots & \ddots & \vdots \\
x_{r,N-P+p,q} & x_{r,N-P+p,q+1} & \cdots & x_{r,N-P+p,K-Q+q}
\end{bmatrix} \quad (16)
$$

After performing the 2-D DFT, the spatial-temporal data in (16) is transformed into the angle-Doppler domain, realizing the dimension reduction both in space domain and time domain. Suppose that the position to be detected is located at the u' th angle gate ($1 \le u' \le N-P+1$) and the v' th Doppler gate ($1 \le v' \le K-Q+1$). Let $u = u' - (N-P+1)/2$, and $v = v' - (K-Q+1)/2$. Then the relationship between u and f_s, v and f_a can be, respectively, expressed as

$$
u/(N-P+1) = d \cdot f_s, \quad v/(K-Q+1) = T_{PRT} \cdot f_a \quad (17)
$$

Then, the echo signal in the angle-Doppler domain is

$$
y_{r,p,q}(u,v) = \sum_{n=0}^{N-P} \sum_{k=0}^{K-Q} \left\{ \begin{array}{l} X_{r,p,q}(n+1,k+1) \\ \times \exp\left[-j2\pi\left(\dfrac{un}{N-P+1} + \dfrac{vk}{K-Q+1} \right) \right] \end{array} \right\} \quad (18)
$$

where $X_{r,p,q}(n+1,k+1)$ means the element at the $(n+1)$th row and the $(k+1)$th column.

Assume that 2-D sliding window is performed M times in a specific mode ($M \le PQ$) (the architecture of sliding window trajectory is discussed in Section III-C). The symbols p and q corresponding to the m th spatial-temporal 2-D sliding window are denoted as p_m and q_m, respectively. Then the data vector of the r th range ring in this sliding window mode is noted as

$$Y_{r,u,v} = \begin{bmatrix} y_{r,p_1,q_1}(u,v) \\ \vdots \\ y_{r,p_M,q_M}(u,v) \end{bmatrix} \tag{19}$$

The dimension-reduced clutter and noise covariance matrix can be expressed as

$$\hat{R}_{cn,u,v} = \frac{1}{N_Y} \sum_{i=1}^{N_Y} Y_{r_i,u,v} Y_{r_i,u,v}^H \tag{20}$$

where N_Y is the number of training samples along range dimension, and r_i denotes the index of range ring corresponding to the i th training sample.

Then, the clutter suppression weight vector can be calculated via the following cost function:

$$\begin{cases} \min \ w_{u,v}^H \hat{R}_{cn,u,v} w_{u,v} \\ s.t. \ w_{u,v}^H \tilde{a}_{target,u,v} = 1 \end{cases} \tag{21}$$

where $\tilde{a}_{target,u,v}$ denotes the target steering vector, i.e.

$$\tilde{a}_{target,u,v}$$
$$= \begin{bmatrix} 1 \\ \exp\left[j2\pi(p_2-p_1)df_{s,target} + j2\pi(q_2-q_1)T_{PRT}f_{a,target} \right] \\ \vdots \\ \exp\left[j2\pi(p_M-p_1)df_{s,target} + j2\pi(q_M-q_1)T_{PRT}f_{a,target} \right] \end{bmatrix} \otimes 1$$

$$= \begin{bmatrix} 1 \\ \vdots \\ \exp\left[j2\pi \dfrac{(p_M-p_1)u}{N-P+1} + j2\pi \dfrac{(q_M-q_1)v}{K-Q+1} \right] \end{bmatrix} \tag{22}$$

It should be noted that different from the traditional STAP algorithms, only one angle-Doppler channel is exploited for each set of data obtained by 2-D sliding window, and thus, the target steering vector of each set of data is 1. The total target steering vector $\tilde{a}_{target,u,v}$ only contains the spatial-temporal phase difference between these sets of data, which can be obtained from the relationship between the echo signal corresponding to the 1st 2-D sliding window and that corresponding to the m th 2-D sliding window, i.e.

$$\begin{aligned} S_{rn,m}(r,f_s,f_a) &= \mathscr{F}_{2D}\left[s_{rn,m}(r,d_n,t_m) \right] \\ &= S_{rn,1}(r,f_s,f_a)\exp\left[j2\pi(p_m-p_1)df_{sa} \right] \\ &\quad \times \exp\left[j2\pi(q_m-q_1)T_{PRT}f_a \right] \end{aligned} \tag{23}$$

where $s_{rn,m}$ and $S_{rn,m}$ denote the echo signals corresponding to the mth 2-D sliding window in the space-time domain and in the angle-Doppler domain, respectively, and $\mathscr{F}_{2D}$ represents the 2-D Fourier transform operation.

In addition, it can be observed from (22) and (23) that, the clutter components with different spatial frequencies and Doppler frequencies will exhibit different steering vectors from the target steering vector $\tilde{a}_{target,u,v}$. Therefore, the leakage component effects can be alleviated since the spatial-temporal vector mismatch with respect to the leakage clutter components occurs, and then the adaptive clutter filtering in (21) can effectively suppress the leakage components, improving the clutter cancelation robustness under the low angle-Doppler resolution case. The processing architecture of the proposed algorithm is shown in Fig. 5.
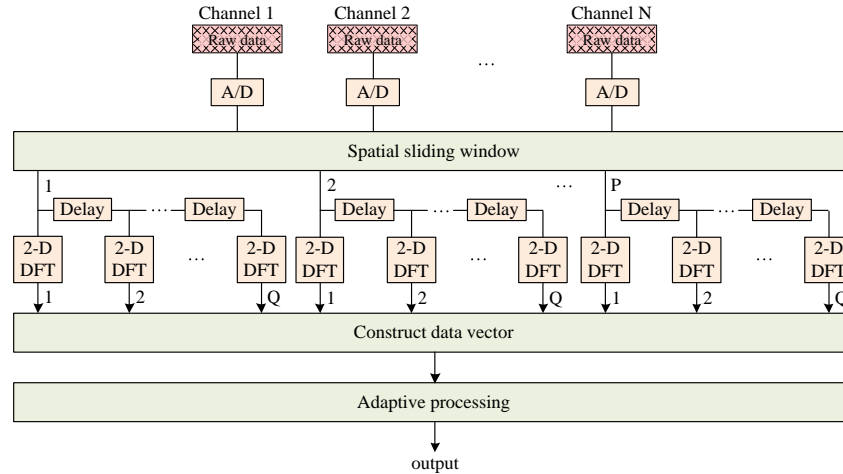

Fig. 5. Processing architecture of the proposed algorithm.

The clutter suppression weight vector can be, then, obtained as

$$w_{u,v} = \frac{\hat{R}_{cn,u,v}^{-1} \tilde{a}_{target,u,v}}{\tilde{a}_{target,u,v}^H \hat{R}_{cn,u,v}^{-1} \tilde{a}_{target,u,v}} \tag{24}$$

According to (18)~(20), (22), and (24), the clutter suppression weight vector of each detected position can be calculated, and the clutter suppression result can be finally given by

$$z_{r,u,v} = w_{u,v}^H Y_{r,u,v} \tag{25}$$

By traversing the Doppler channels to be detected, the detection results with respect to each target radial velocity can be obtained, realizing the moving target detection. The relationship between the target spatial frequency and the target spatial angles can be noted as $f_{s,target} = \sin\varphi_{target}\cos\theta_{target}/\lambda$, where φ_{target} and θ_{target} denote the target elevation angle and azimuth angle with respect to the radar antenna array,

respectively. Obviously, when the radar main beam works in a side-looking mode, i.e. $\theta_{target} = 90°$, one has $f_{s,target} = 0$.
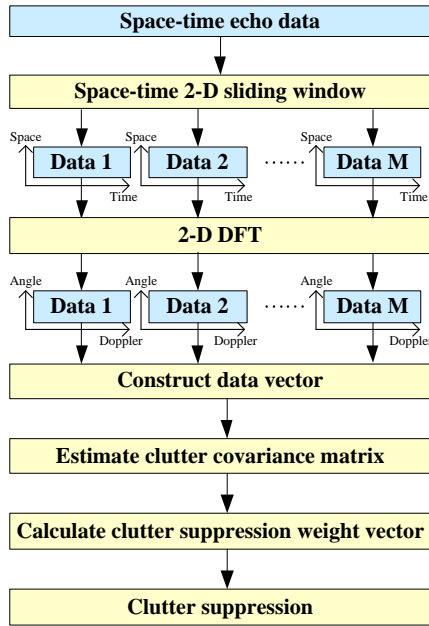

Fig. 6. Flow chart of the proposed algorithm.

The flow chart of the proposed algorithm is shown in Fig. 6, and the procedures of the proposed algorithm are mainly summarized in Table 1.

Table 1 Procedures of the proposed algorithm

Step 1) Obtain M sets of spatial-temporal data by sliding the spatial-temporal 2-D sliding window for M times.

Step 2) Transform these M sets of spatial-temporal data into the angle-Doppler domain by using 2-D DFT.

Initialize the current angle-Doppler gate as the u_0 th angle gate and the v_0 th Doppler gate.

Repeat

    Step 3) Construct the data vector and estimate the clutter covariance matrix based on the range i.i.d training samples.

    Step 4) Calculate the clutter suppression weight vector and obtain the clutter suppression result.

    Step 5) Process the next angle-Doppler gate.

Until all the angle-Doppler gates to be detected are processed.

Output the processing results.

Remark: According to the principle of the proposed method, it is apparent that, when $P = 1$ and $Q = 1$, the proposed method reduces into the simple 2-D DFT based angle-Doppler domain method, which is computationally efficient at the sacrifice of clutter spatial filtering performance (see the processing results in Section IV-B). When $P = N$ and $Q = 1$, the proposed method reduces to a well-known post-Doppler method named factored-STAP [25] since the DFT processing along spatial domain is invalid. When $P = N$ and $Q = 3$, the proposed method reduces to the famous F$A method [26] since multiple sets of temporal-spatial data are applied to realize the jointly adaptive processing. In addition, when $P = N$ and $Q = K$, the proposed method is the same as that of the whole-dimensional STAP. Therefore, the 2-D DFT based STAP algorithm, the factored-STAP algorithm, the F$A algorithm, and the whole-dimensional STAP algorithm are the special cases of the

proposed method. It should be noted that when the target spatial steering vector mismatch is present in (24), the proposed method will suffer from the target detection performance degradation, which is analyzed in Appendix.

C. Sliding Window Modes

In this section, the sliding window modes are discussed. Suppose that the times of space-domain window sliding and time-domain window sliding are P and Q, respectively, and $P \cdot Q$ sets of spatial-temporal data can be obtained (see Fig. 4). Two modes of window sliding will be defined in the following.

Mode 1: Utilize the whole $P \cdot Q$ sets of spatial-temporal data to realize the joint data processing, i.e., $M = P \cdot Q$. For simplicity, suppose that $P = Q = 3$, and the sketch map of this sliding window mode is shown in Fig. 7. The dimension of covariance matrix becomes $PQ \times PQ$, and the proposed algorithm in this mode is defined as $2\,\text{DSW}_{\square,P,Q}$ for simplicity.
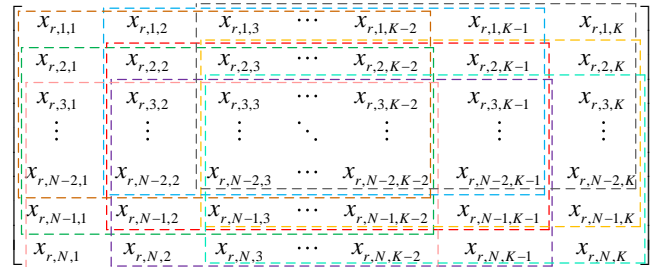

Fig. 7. Sketch map of $2\text{DSW}_{\square,3,3}$.

Then the data vector corresponding to the r th range ring can be expressed as

$$Y_{r,u,v} = \begin{bmatrix} y_{r,1,1}(u,v) \\ \vdots \\ y_{r,1,Q}(u,v) \\ y_{r,2,1}(u,v) \\ \vdots \\ y_{r,2,Q}(u,v) \\ \vdots \\ y_{r,P,1}(u,v) \\ \vdots \\ y_{r,P,Q}(u,v) \end{bmatrix} \tag{26}$$

Mode 2: Assume that $M = P + Q - 1$. For simplicity, suppose that $P = Q = 3$, and the sketch map of sliding window mode is shown in Fig. 8. The dimension of covariance matrix is $(P+Q-1) \times (P+Q-1)$ now, and the proposed algorithm in this mode is defined as $2\,\text{DSW}_{+,P,Q}$.
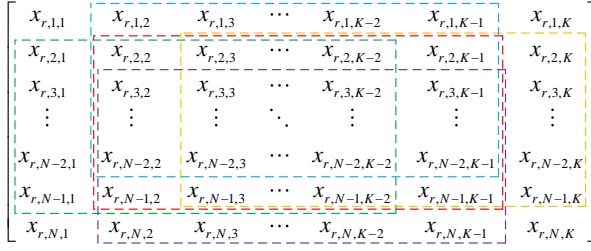
Fig. 8. Sketch map of $2\mathrm{DSW}_{+,3,3}$.

The data vector corresponding to the r th range ring in this mode can be expressed as

$$
Y_{r,u,v} = \begin{bmatrix}
y_{r,1,\left\lfloor\frac{Q+1}{2}\right\rfloor}(u,v) \\
\vdots \\
y_{r,\left\lfloor\frac{P-1}{2}\right\rfloor,\left\lfloor\frac{Q+1}{2}\right\rfloor}(u,v) \\
y_{r,\left\lfloor\frac{P+1}{2}\right\rfloor,1}(u,v) \\
\vdots \\
y_{r,\left\lfloor\frac{P+1}{2}\right\rfloor,Q}(u,v) \\
y_{r,\left\lfloor\frac{P+1}{2}\right\rfloor+1,\left\lfloor\frac{Q+1}{2}\right\rfloor}(u,v) \\
\vdots \\
y_{r,P,\left\lfloor\frac{Q+1}{2}\right\rfloor}(u,v)
\end{bmatrix}
\qquad (27)
$$

where $\lfloor\bullet\rfloor$ denotes the rounding down operation.

The clutter suppression performance corresponding to these two sliding window modes will be analyzed in Section IV.

D. Computational Complexity Analysis

In this section, we compare the computational complexity of the proposed algorithm with some typical STAP algorithms, such as full-dimensional optimal STAP [11], factored approach (FA) [25], order-2 EFA [25], F\$A [26], JDL [29], STMB [31], and ΣΔ-STAP [27]. For these STAP based algorithms, the main time-consuming computations include the Fourier transform, covariance matrix estimation, clutter suppression weight vector calculation, and clutter suppression. Suppose that the numbers of pulses, spatial channels, and range training samples are denoted by K , N , and N_Y , respectively. For the JDL algorithm, assume that the size of localized processing region is 3×3 . For the STMB algorithm, the number of spatial auxiliary channels and the number of temporal auxiliary channels are chosen as 2 and 2, respectively. And for the proposed algorithm, $2\mathrm{DSW}_{+,3,3}$ is taken as an example (see the sketch map in Fig. 8). The detailed computational costs of these algorithms are listed in Table 2, where it is clearly observed that although the optimal STAP possesses the optimal clutter suppression quality at the case of enough i.i.d. samples, it is extremely time-consuming. After implementing the Doppler localization, the FA, order-2 EFA, and F\$A algorithms have the moderate

computational complexities. Compared to the above algorithms, the JDL, the STMB, and the proposed algorithm are computationally efficient because these algorithms usually exhibit lower clutter degree of freedom after performing the clutter localization along both temporal and spatial dimensions.

Table 2 Computational costs of typical STAP algorithms

	Data domain transformation	Covariance matrix estimation	Clutter suppression weight vector calculation	Clutter suppression
Optimal STAP	/	$(NK)^2 N_Y$	$3(NK)^3 + (NK)^2 K$	$(NK)N_Y K$
FA	$\frac{N_Y NK}{2}\log_2 K$	$N^2 N_Y K$	$3N^3 K + N^2 K$	$NN_Y K$
Order-2 EFA	$\frac{N_Y NK}{2}\log_2 K$	$(3N)^2 N_Y K$	$3(3N)^3 K + (3N)^2 K$	$3NN_Y K$
F\$A	$\frac{3N_Y NK}{2}\log_2 K$	$(3N)^2 N_Y K$	$3(3N)^3 K + (3N)^2 K$	$3NN_Y K$
JDL$_{3\times3}$	$\frac{N_Y NK}{2}\log_2 N + \frac{3N_Y K}{2}\log_2 K$	$9^2 N_Y K$	$3\times9^3 K + 9^2 K$	$9N_Y K$
STMB$_{2+2}$	$\frac{N_Y NK}{2}\log_2 N + \frac{3N_Y K}{2}\log_2 K$	$5^2 N_Y K$	$3\times5^3 K + 5^2 K$	$5N_Y K$
ΣΔ-STAP	$N_Y K\log_2 K$	$6^2 N_Y K$	$3\times6^3 K + 6^2 K$	$6N_Y K$
$2\mathrm{DSW}_{+,3,3}$	$\frac{5N_Y NK}{2}\log_2 N + \frac{5N_Y K}{2}\log_2 K$	$5^2 N_Y K$	$3\times5^3 K + 5^2 K$	$5N_Y K$

Suppose that the number of training samples is 200. After 1000 Monte Carlo simulations, the curves of the computational load and the simulated running time varying with the numbers of pulses and spatial channels are shown in Fig. 9 and Fig. 10, respectively, where N is set as 16 in Fig. 9(a) and Fig. 10(a), K is set as 90 in Fig. 9(b) and Fig. 10(b) (The processor of our computer is: Intel Core i7-9750H CPU at 2.6 GHz, and the RAM is 8 GB). From the figures, it is observed that the computational load of the order-2 EFA is close to that of F\$A algorithm with three taps. In addition, the computational loads of the JDL, the STMB, the ΣΔ-STAP, and the proposed algorithm are lower than those of the other algorithms, which is beneficial for real-time processing in a SEWR system. Furthermore, the proposed algorithm exhibits better clutter suppression performance than those of JDL, STMB and ΣΔ-STAP algorithms, which will be analyzed in Section IV. As a conclusion, the proposed algorithm can achieve a well balance with the consideration of computational complexity and clutter suppression performance.
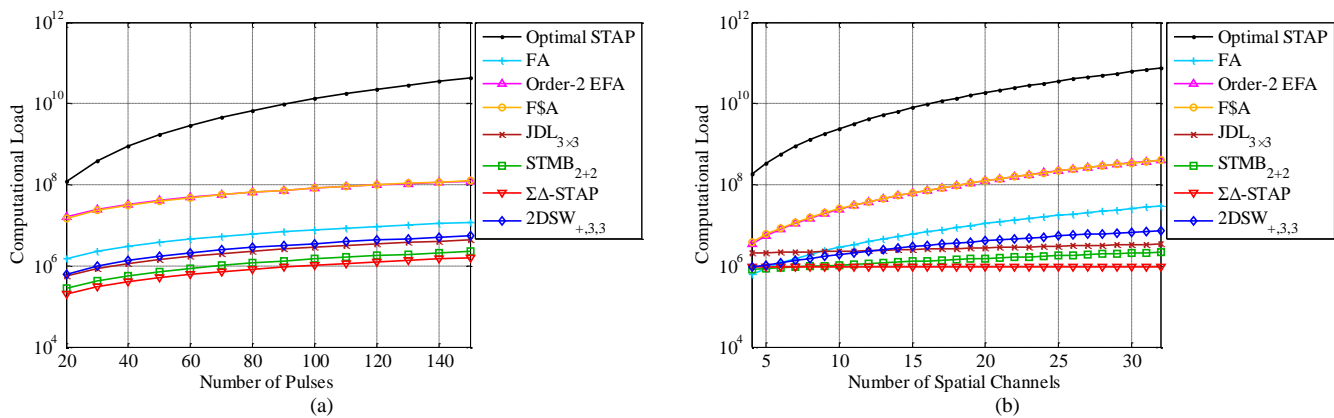
Fig. 9. Computational load curves of the proposed algorithm and typical STAP algorithms. (a) Computational load curves varying with the number of pulses. (b) Computational load curves varying with the number of spatial channels.
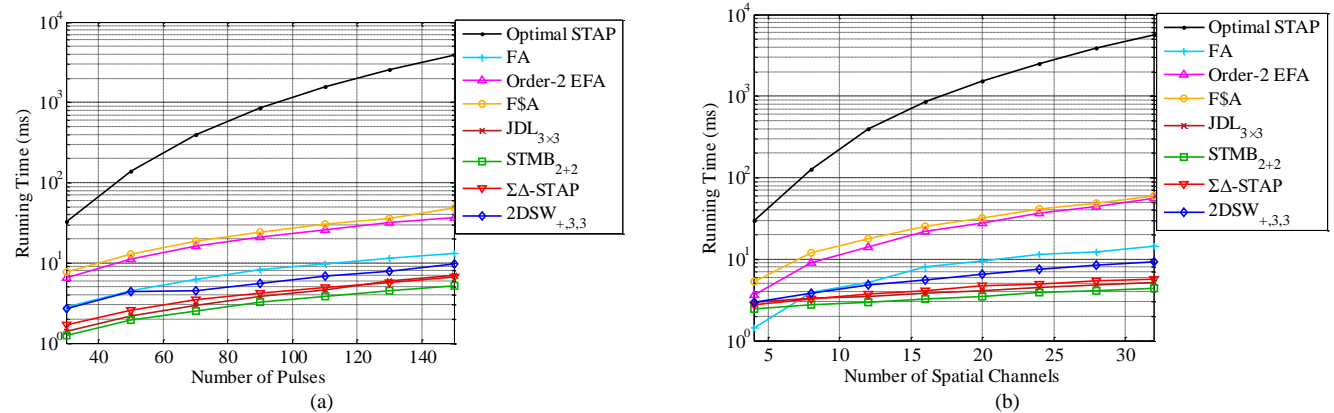

Fig. 10. Running time curves of the proposed algorithm and typical STAP algorithms. (a) Running time curves varying with the number of pulses. (b) Running time curves varying with the number of spatial channels.

IV. SIMULATED AND REAL-MEASURED DATA ANALYSIS

A. Simulation Results

In this section, the clutter suppression performance of the proposed algorithm is analyzed according to the simulation results. In this simulation, the L-band SEWR works in a side-looking mode, and the radar system parameters refer to the American large L-band space-based radar (LLSBR) project in [46], as listed in Table 3 and Table 4. In addition, the desert terrain is chosen as the observation scene, which is modeled by the Morchin model [47] with the consideration of the Rayleigh distribution. The target parameters are shown in Table 5.

Table 3 Radar system parameters

Platform height	508 km
Radar frequency	1.26 GHz
Range bandwidth	3 MHz
Range sampling frequency	3.6 MHz
Receiver noise bandwidth	3.6 MHz
Pulse repetition frequency	3000 Hz
Number of pulses in a CPI	90
Elevation angle of beam center	45 °
Azimuth angle of beam center	90 °
Average transmitting power	4 kW
Number of spatial receiving channels	16
Channel amplitude error	0.5 dB (3σ)
Channel phase error	5 °(3σ)
Noise factor	2 dB
System loss	11 dB

Table 4 Antenna parameters

Antenna installation angle	45 °
Azimuth antenna size	50 m
Elevation antenna size	2 m
Transmitting antenna gain	42.1 dB
Receiving antenna gain	42.1 dB
Transmitting azimuth and elevation weighting	-13 dB/-13 dB (rectangle weighting)
Receiving azimuth and elevation weighting	-40 dB/-20 dB (Chebyshev weighting)

Table 5 Target parameters

	Range gate number	Radar cross section	Radial velocity
Target 1	500	20 m²	20 m/s
Target 2	600	20 m²	50 m/s
Target 3	700	20 m²	100 m/s

Fig. 11~Fig. 13 show the range-Doppler spectrum, the averaged Doppler spectrum, and the power spectrum of the simulated clutter scene. From Fig. 11, it can be seen that, due to the high-speed motion of radar platform, the clutter Doppler spectrum broadens severely, where the main-lobe clutter width is calculated as 265 Hz, which is close to the theoretical value of 282 Hz according to the radar system parameters listed in Table 3 and Table 4. After performing the amplitude averaging on Fig. 11 along range dimension, the shape of the range-averaged clutter power shown in Fig. 12 is modulated by the transmitting and receiving two-way antenna patterns, where the first pair of side-lobe levels are about 13.2 dB lower than

the main-lobe clutter level, indicating that the contribution of receiving antenna pattern is much smaller than that of transmitting one since the received antenna panel is divided into 16 sub-channels along azimuth. That is to say, when a moving target is close to the main-lobe clutter regions or the neighbor side-lobe clutter regions, the two-way antenna pattern weighting may not be sufficient to decrease the clutter power, i.e., the moving target signal should compete with the strong clutter components with a preset detection threshold, significantly degrading the moving target output SCNR. Therefore, in order to improve the SEWR detection performance, the effective clutter suppression becomes necessary. From the space-time power spectrum in Fig. 13, the multi-channel clutter is represented as an oblique line in the 2-D angle-Doppler plane, indicating that the efficient and effective clutter filtering in the angle-Doppler domain becomes possible.
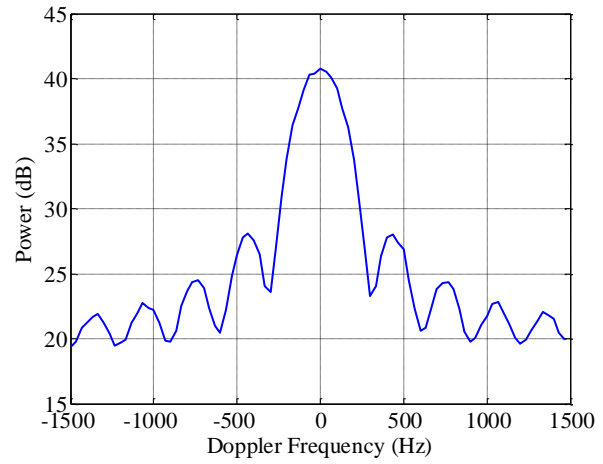

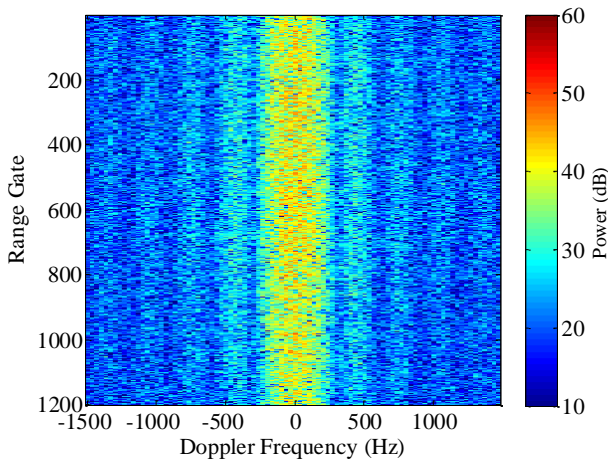Fig. 12. Averaged Doppler spectrum of the simulated clutter.

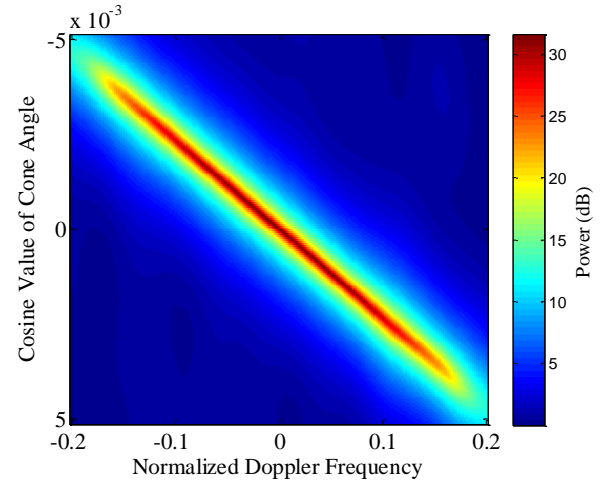Fig. 11. Range-Doppler spectrum of the simulated clutter.
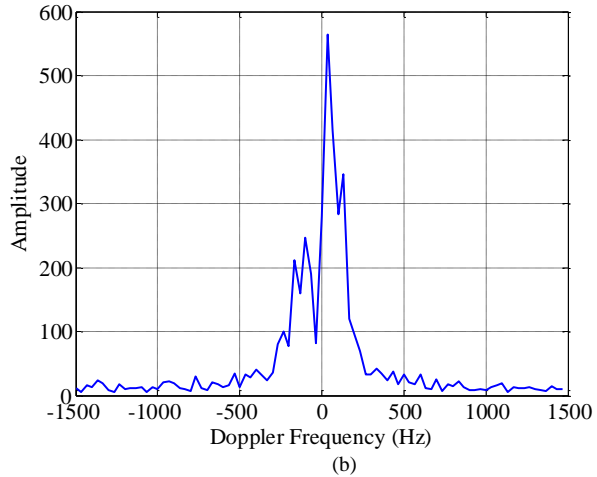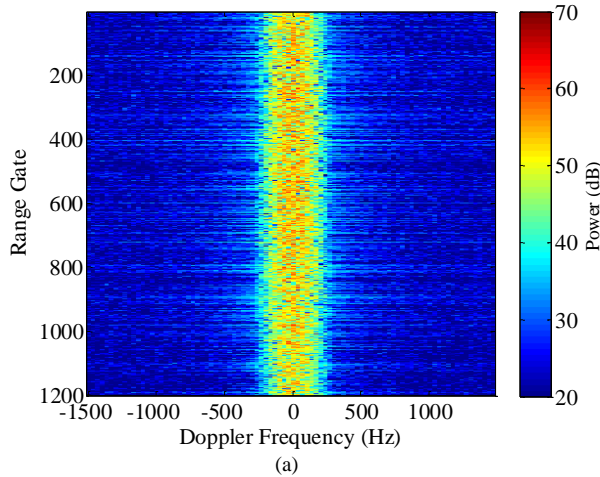

Fig. 13. Space-time power spectrum of the simulated clutter.
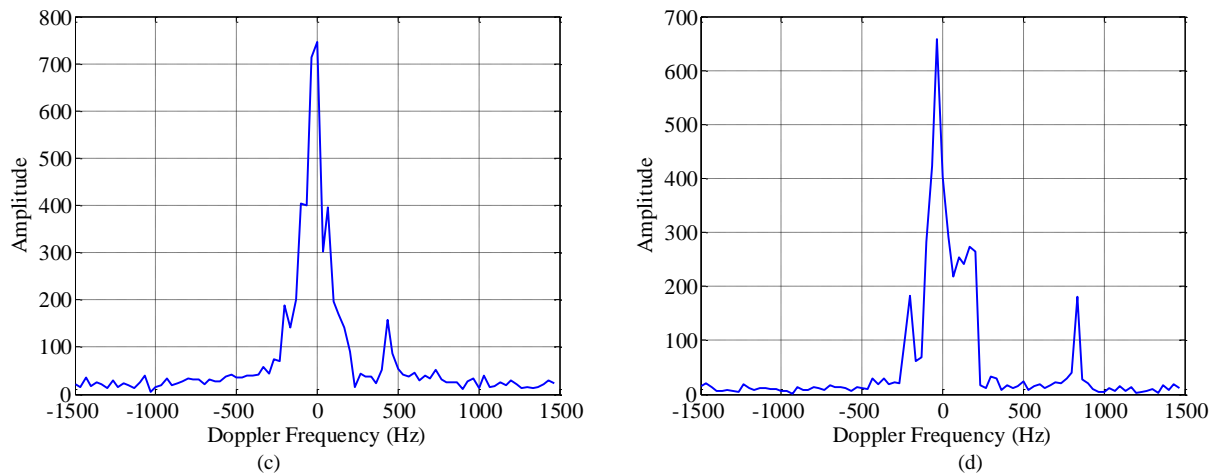

(a)

(b)

Fig. 14. Processing results by using the non-adaptively spatial synthesizing technique with respect to these 16 spatial sub-channels. (a) Range-Doppler spectrum. (b) 1-D slice with respect to the 500th range gate. (c) 1-D Doppler slice figure with respect to the 600th range gate. (d) 1-D slice with respect to the 700th range gate.

Fig. 14 shows the non-adaptively spatial synthesizing results with respect to these 16-channel radar data, including the range-Doppler spectrum and the Doppler slice figures associated with the 500th, 600th, and 700th range gates. Obviously, due to the platform high-speed motion, the clutter suppression performance is not satisfied and the slow-moving targets cannot be effectively detected in the main-lobe clutter region, although the side-lobe clutter level is suppressed by the transmitting and receiving two-way antenna patterns. Therefore, for the moving target detection in a SEWR system, only applying the deeply weighting technique on receiving antenna pattern (the transmitting antenna pattern usually involves the uniform weight in order to improve the transmitting power of a SERW system) to realize the weak target detection may be invalid in the case of the broadened main-lobe clutter, which means that the application of STAP technique is necessary for the moving target detection in a SERW system.

After using the proposed 2DSW$_{+,3,3}$ algorithm, the range-Doppler spectrum and the 1-D Doppler slice figures of the 500th, 600th, and 700th range gates are shown in Fig. 15(a)

~ Fig. 15(d), respectively. From the figures, it can be clearly observed that, most of the main-lobe clutter components are suppressed effectively, and these three moving targets can be effectively detected, with the output SNRs listed in Table 6. The statistical output SNRs are close to the ideal ones calculated according to the parameters in Table 3~Table 5, indicating that the target output power is effectively retained. It should be noted that the output SNRs of target 2 and target 3 are slightly lower than the ideal ones due to the picket fence effect. In addition, the clutter component in the radar beam center position is also retained in order to keep the target output power as much as possible, which is different from the spatial mismatch processing in a multichannel SAR-GMTI system.

Table 6 Target output SNRs and ideal SNRs

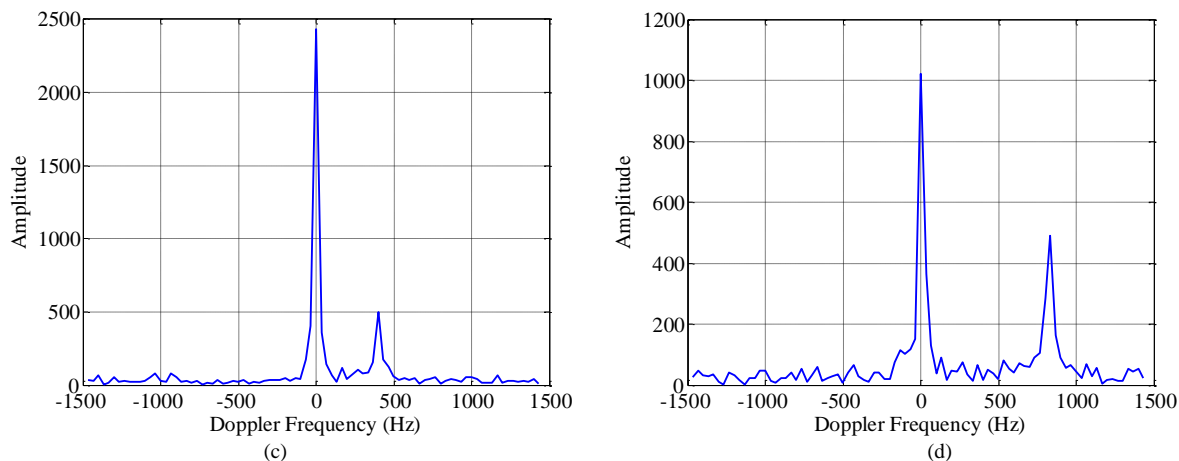| Targets	Output SNR	Ideal SNR
Target 1	25.6 dB	26.0 dB
Target 2	23.3 dB	25.9 dB
Target 3	23.2 dB	25.7 dB

(a)

(b)
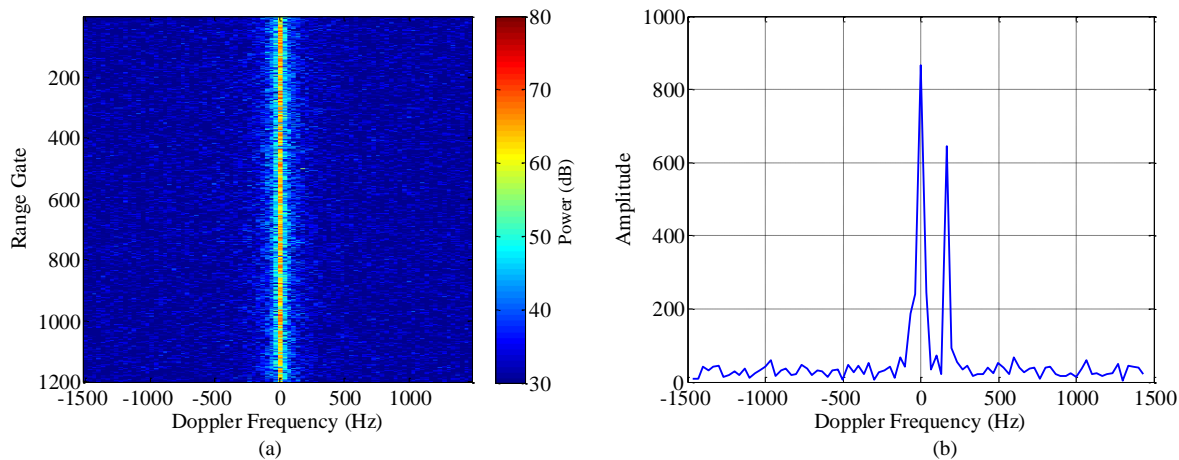
Fig. 15. Processing results by using the proposed $2DSW_{+,3,3}$ algorithm. (a) Range-Doppler spectrum. (b) 1-D Doppler slice figure of the 500th range gate. (c) 1-D Doppler slice figure of the 600th range gate. (d) 1-D Doppler slice figure of the 700th range gate.

B. Detection Performance Analysis

In this section, the clutter suppression performances of different STAP algorithms will be comparatively analyzed according to the simulated data with the same parameters as those listed in Table 3 and Table 4. The clutter suppression performance is evaluated by applying the SCNR as the evaluating indicator.

1) Comparisons of Different Sliding Window Modes

Fig. 16 shows the target output SCNR curves by using the $2DSW_{\square,3,3}$ and $2DSW_{+,3,3}$, where Fig. 16(b) is the local enlarged figure of Fig. 16(a). The average output SCNRs for target radial velocities of 20~50 m/s (regarded as slow-moving target) and 50~170 m/s (regarded as medium- and fast-moving target) are listed in Table 7. From Fig. 16 and Table 7, it can be seen that, the target detection performance of $2DSW_{+,3,3}$ is approximately the same as that of $2DSW_{\square,3,3}$ (the output SCNR difference between these two algorithms is lower than 0.2 dB). However, compared with $2DSW_{\square,3,3}$, the covariance matrix dimension of $2DSW_{+,3,3}$ decreases from 9×9 to 5×5, indicating that the second sliding window mode may be more suitable for the real-time processing in a SEWR system.
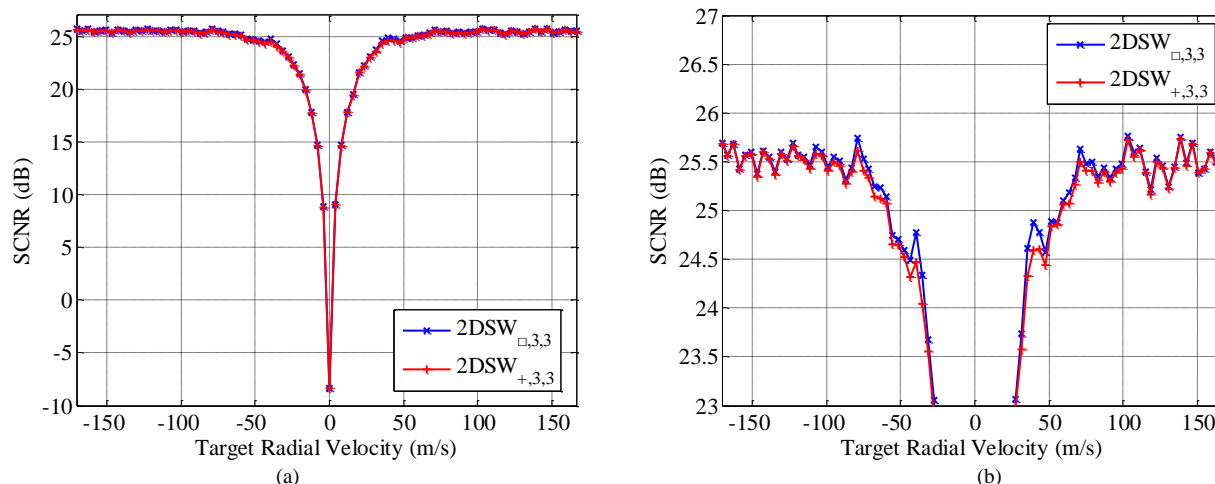

Fig. 16. Output SCNR curves by using the proposed $2DSW_{\square,3,3}$ and $2DSW_{+,3,3}$. (a) Output SCNR curves. (b) Local enlarged figure of Fig. 16(a).

Table 7 Output SCNRs

Methods	Average SCNR for a slow-moving target	Average SCNR for a medium- and fast-moving target
$2DSW_{\square,3,3}$	23.96 dB	25.46 dB
$2DSW_{+,3,3}$	23.79 dB	25.41 dB

Fig. 17 shows the SCNR curves by using $2DSW_{+,5,5}$, $2DSW_{+,5,3}$, $2DSW_{+,3,5}$, $2DSW_{+,3,3}$, and $2DSW_{+,1,1}$. It can be observed from Fig. 17 that, the $2DSW_{+,1,1}$ algorithm without applying the spatial-temporal 2-D sliding window, exhibits an unacceptable clutter filtering performance, indicating the advantage of the proposed 2-D sliding window based STAP method. In addition, the influence of the window sliding times on the clutter suppression performance is relatively small, and the increase of spatial and temporal window sliding times will slightly improve the target detection performance for a slow-moving target, as listed in Table 8. As for a medium- or fast-moving target, the target output SCNRs are approximately the same with the increase of window sliding times. However, with the increasing of the value of time-domain sliding times Q, the computational load is increased. As a result, the $2DSW_{+,3,3}$ algorithm usually provides the adequate performance for the general case, and the $2DSW_{+,5,3}$ algorithm can be chosen when the spatial receiving channels are enough (i.e. more than 5

spatial receiving channels are required to accomplish the spatial window sliding processing).
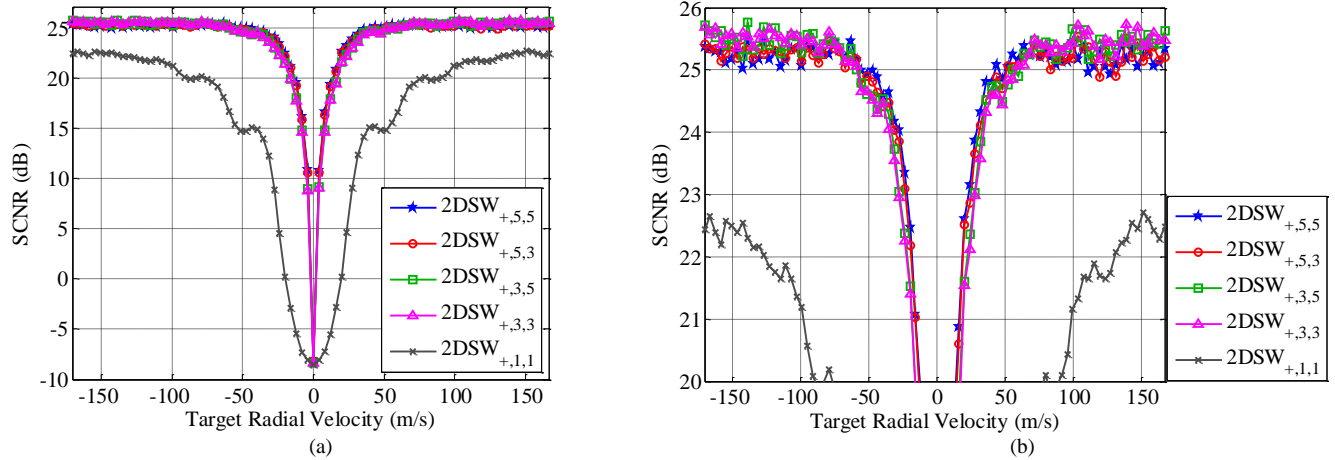

Fig. 17. Output SCNR curves by using $2DSW_{+,5,5}$, $2DSW_{+,5,3}$, $2DSW_{+,3,5}$, $2DSW_{+,3,3}$, and $2DSW_{+,1,1}$. (a) Output SCNR curves. (b) Local enlarged figure of Fig. 17(a).

Table 8 Output SCNRs

Methods	Average SCNR for a slow-moving target	Average SCNR for a medium- and fast-moving target
$2DSW_{+,5,5}$	24.37 dB	25.23 dB
$2DSW_{+,5,3}$	24.19 dB	25.24 dB
$2DSW_{+,3,5}$	23.90 dB	25.40 dB
$2DSW_{+,3,3}$	23.79 dB	25.41 dB
$2DSW_{+,1,1}$	21.04 dB	23.80 dB

2) Comparisons of Different STAP Algorithms

In this section, the clutter suppression performances of $2DSW_{+,5,3}$, F$A [26], order-2 EFA [25], $JDL_{3\times3}$ [29], $STMB_{2+4}$ [31], $\Sigma\Delta$-STAP [27], eigencanceler [19], and optimal STAP [11] are compared via evaluating the target output SCNR. Firstly, the influence of clutter-to-noise ratio (CNR) on the clutter suppression performance of these STAP algorithms is analyzed in the following.

a) Influence of CNR

Fig. 18 shows the SCNR curves by using $2DSW_{+,5,3}$, F$A, order-2 EFA, $JDL_{3\times3}$, $STMB_{2+4}$, $\Sigma\Delta$-STAP, eigencanceler, and optimal STAP where the desert terrain (a relatively low CNR)

is chosen as the observation scene. It should be noted that the available training samples are not enough for the optimal STAP to utilize the full space-time aperture. Therefore, the space-time aperture is reduced when the optimal STAP is applied. Clearly, it can be observed that the performances of $2DSW_{+,5,3}$, F$A, order-2 EFA, eigencanceler, and optimal STAP are relatively robust, while the performances of $JDL_{3\times3}$, $STMB_{2+4}$, and $\Sigma\Delta$-STAP are influenced by the clutter side-lobe to a certain extent. The performance of $\Sigma\Delta$-STAP deteriorates obviously due to the lack of spatial freedom, as listed in Table 9. For the optimal STAP, the performance degrades when the provided i.i.d. training samples are not enough. In addition, the covariance matrix dimension of $2DSW_{+,5,3}$ is 7×7, while the covariance matrix dimensions of the other algorithms applied in this simulation are 48×48 (F$A), 48×48 (order-2 EFA), 9×9 ($JDL_{3\times3}$), 7×7 ($STMB_{2+4}$), and 6×6 ($\Sigma\Delta$-STAP), respectively. As for the eigencanceler, an eigen-decomposition processing should be performed on a covariance matrix with the dimensions of 1440×1440, indicating its high computational load. As a result, the proposed algorithm can achieve a good balance between the clutter suppression performance and the computational complexity.
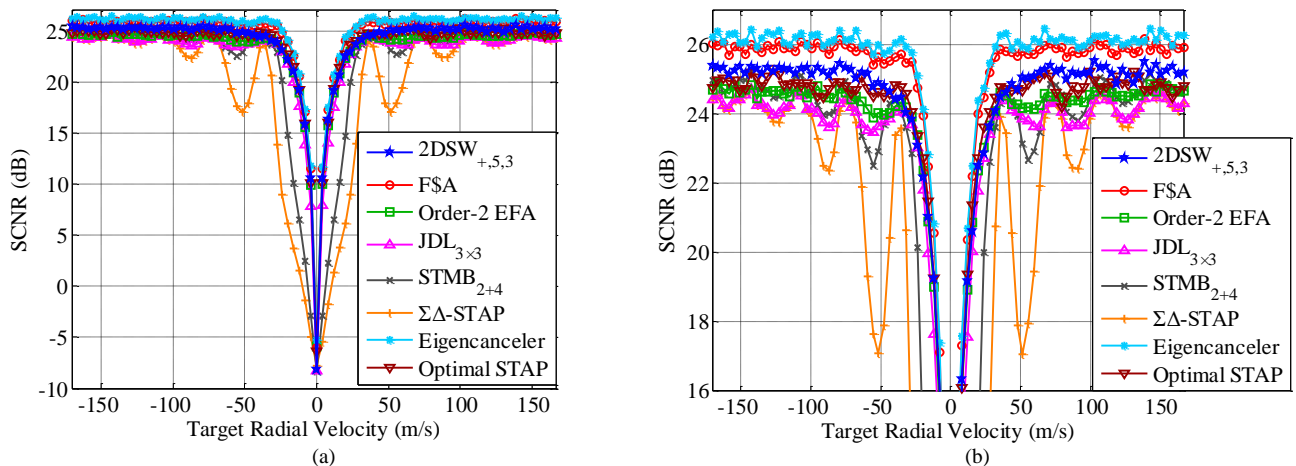
Fig. 18. Output SCNR curves by using the $2\text{DSW}_{+,5,3}$, F$A, order-2 EFA, $\text{JDL}_{3\times3}$, STMB_{2+4}, $\Sigma\Delta$-STAP, eigencanceler, and optimal STAP. (a) Output SCNR curves. (b) Local enlarged figure of Fig. 18(a).

Table 9 Output SCNRs

Methods	Average SCNR for a slow-moving target	Average SCNR for a medium- and fast-moving target
$2\text{DSW}_{+,5,3}$	24.19 dB	25.24 dB
F$A	25.42 dB	25.90 dB
Order-2 EFA	23.97 dB	24.57 dB
$\text{JDL}_{3\times3}$	23.75 dB	24.16 dB
STMB_{2+4}	23.25 dB	24.51 dB
$\Sigma\Delta$-STAP	20.04 dB	23.70 dB
Eigencanceler	25.78 dB	26.18 dB
Optimal STAP	24.37 dB	24.86 dB

Fig. 19 shows the SCNR curves by using $2\text{DSW}_{+,5,3}$, F$A, order-2 EFA, $\text{JDL}_{3\times3}$, STMB_{2+4}, $\Sigma\Delta$-STAP, eigencanceler, and optimal STAP, where the hill terrain (a relatively high CNR) is chosen as the observation scene. And Table 10 provides the average SCNRs of these algorithms. From the figures and table, it can be seen that the proposed $2\text{DSW}_{+,5,3}$ algorithm still has a good clutter suppression performance in this high CNR scene, while the performances of STMB_{2+4} and $\Sigma\Delta$-STAP degrade significantly due to their limited clutter suppression capabilities. Therefore, the proposed algorithm exhibits the robustness to the different observed scene types.
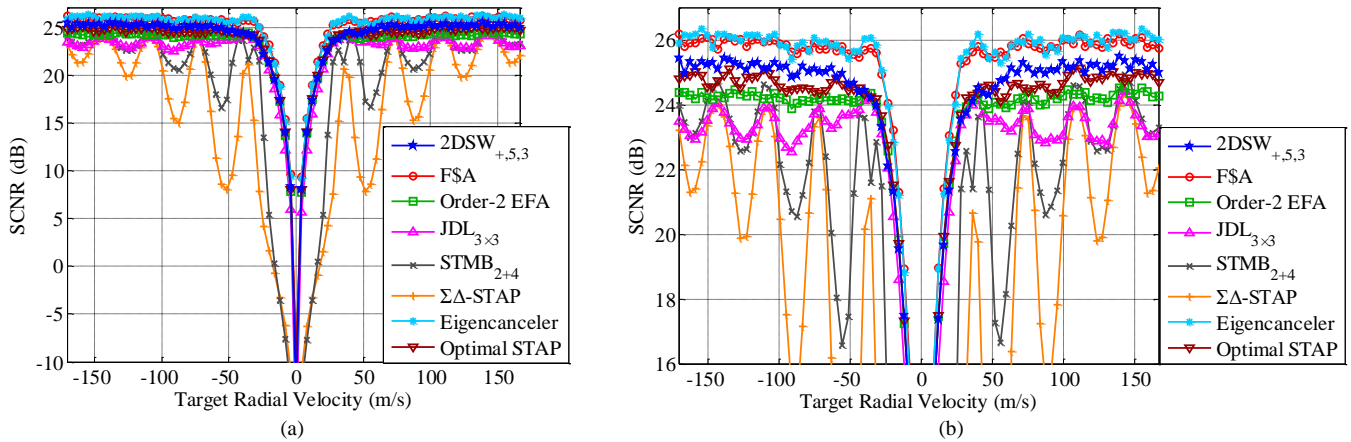

(a)

(b)

Fig. 19. Output SCNR curves by using the $2\text{DSW}_{+,5,3}$, F$A, order-2 EFA, $\text{JDL}_{3\times3}$, STMB_{2+4}, $\Sigma\Delta$-STAP, eigencanceler, and optimal STAP. (a) Output SCNR curves. (b) Local enlarged figure of Fig. 19(a).

Table 10 Output SCNRs

	Average SCNR for slow-moving target	Average SCNR for medium- and fast-moving target
$2\text{DSW}_{+,5,3}$	23.87 dB	25.16 dB
F$A	25.26 dB	25.89 dB
Order-2 EFA	23.80 dB	24.25 dB
$\text{JDL}_{3\times3}$	23.47 dB	23.39 dB
STMB_{2+4}	21.48 dB	22.95 dB
$\Sigma\Delta$-STAP	15.73 dB	21.54 dB
Eigencanceler	25.42 dB	26.00 dB
Optimal STAP	24.00 dB	24.73 dB

b) Influence of the Number of Spatial Channels

Fig. 20. SCNRs varying with the number of channels after using $2\text{DSW}_{+,5,3}$,

F$A, order-2 EFA, $\text{JDL}_{3\times3}$, STMB_{2+4}, $\Sigma\Delta$-STAP, eigencanceler, and optimal STAP.

Suppose that the target radial velocity is 50 m/s. Fig. 20 shows the output SCNR curves by using $2\text{DSW}_{+,5,3}$, F$A, order-2 EFA, $\text{JDL}_{3\times3}$, STMB_{2+4}, $\Sigma\Delta$-STAP, eigencanceler, and optimal STAP. It can be observed that with the increase of spatial receiving channels, the target output SCNR increases due to the fact that the more the spatial receiving channels, the larger the target SNR as well as the better the clutter suppression performance. In addition, the SCNR variation tendencies of these algorithms are similar, due to the fact that all these algorithms are affected by the number of spatial receiving channels.

C. Real-Measured Radar Data Analysis

Table 11 Airborne radar system parameters

Radar frequency	2.3 GHz
Number of pulses in a CPI	100
Number of spatial receiving channels	5

In this section, the clutter suppression performance of the proposed algorithm and the other typical dimension-reduced STAP algorithms will be comparatively analyzed according to a set of real-measured multi-channel radar data, which was recorded by an airborne surveillance radar system, with the system parameters listed in Table 11.

3) Comparison of Different STAP Algorithms

Fig. 21(a) and Fig. 21(b) show the range-Doppler spectrum and power spectrum of this real-measured radar data, respectively. From the figures, we can see that the clutter spectrum is significantly broadened due to the platform motion, causing the moving target difficult to be detected; thus, the effective clutter suppression is necessary for the moving target detection in this real-measured airborne data.
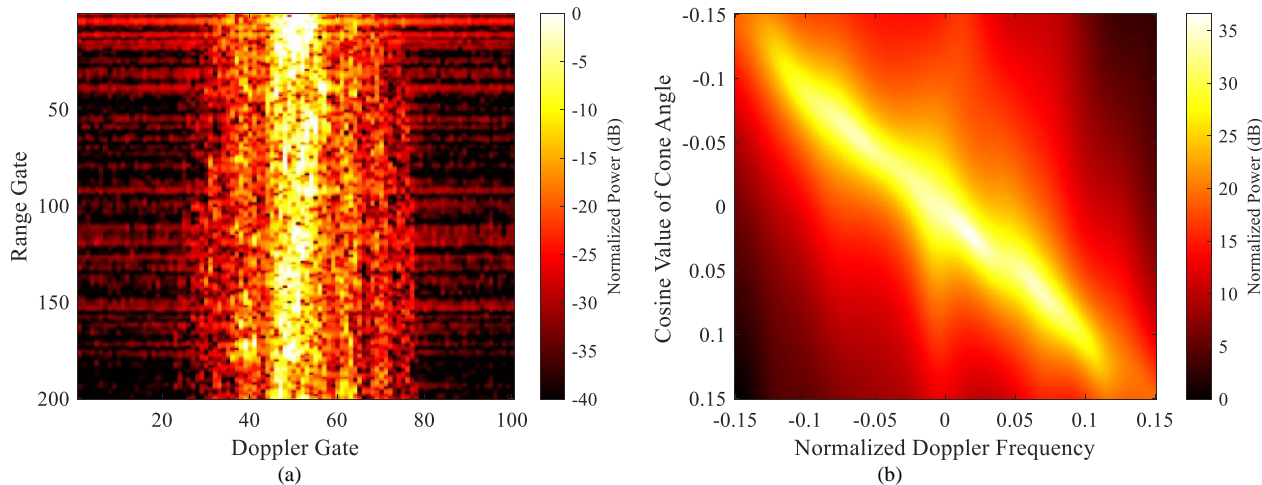

Fig. 21. Multichannel real-measured data processing. (a) Range-Doppler spectrum of the real-measured airborne data. (b) Power spectrum of the real-measured clutter.

By applying the generalized inner product non-homogeneity detection (GIP NHD) [48]-[50] to realize the training sample selection, Fig. 22 shows the clutter suppression results by using the proposed $2\,\mathrm{DSW}_{+,3,3}$ algorithm, from which it can be observed that most of the main-lobe clutter components is effectively filtered by using the proposed algorithm and a moving target can be well detected by applying the constant false alarm rate (CFAR) technique.
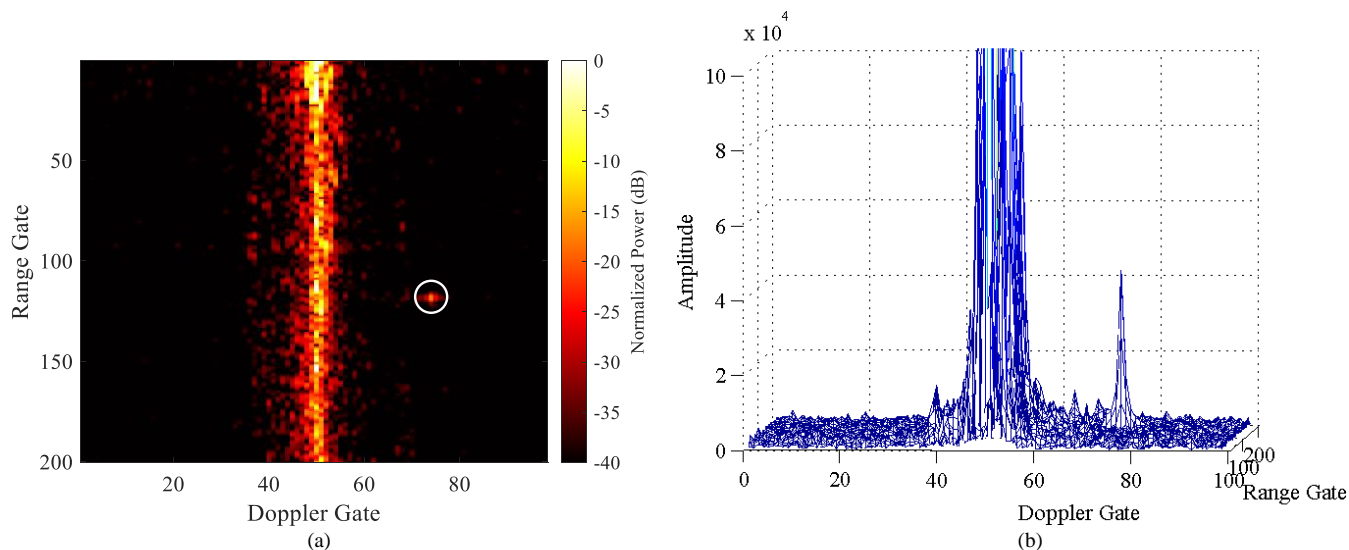

Fig. 22. Range-Doppler spectrum by applying the proposed $2\,\mathrm{DSW}_{+,3,3}$ algorithm. (a) Range-Doppler spectrum. (b) Mesh figure of range-Doppler spectrum.

After applying GIP NHD, Fig. 23 shows the clutter suppression results by using GIP NHD and $2\,\mathrm{DSW}_{+,3,3}$, F$A, order-2 EFA, $\mathrm{JDL}_{3\times3}$, STMB_{2+4}, and $\Sigma\Delta$-STAP algorithms, where Figs. 23(a), (c), (e), (g), (i), (k) are the 1-D Doppler slice figures of the clutter suppression results of the 118th range gate (i.e., the range gate where this moving target is located at), and Figs. 23(b), (d), (f), (h), (j), (l) are the 1-D range slice figures of the clutter suppression results of the 74th Doppler gate (i.e., the Doppler gate where the target is located at). It should be noted that both the full-dimensional optimal STAP and eigencanceler cannot effectively work due to the small number of training samples. From the figures, it can be seen that the target is effectively detected after applying the proposed algorithm and the other typical dimension-reduced STAP algorithms, while the proposed algorithm and F$A exhibit relatively high SCNRs, as listed in Table 12. Compared with F$A, the proposed algorithm has a relatively low computational complexity, indicating its application potential in practical engineering.
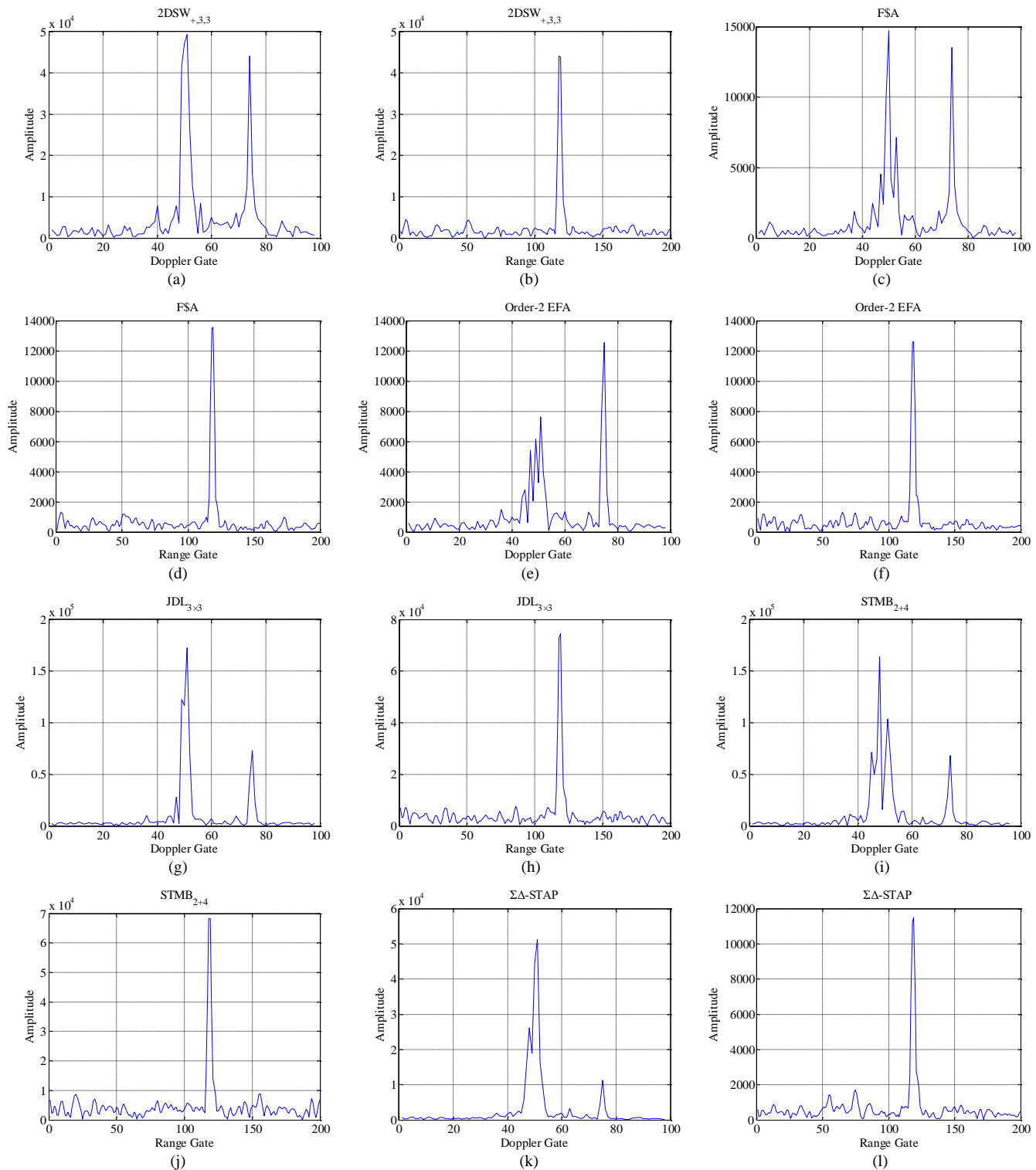
Fig. 23. 1-D slice figures by using the proposed algorithm and other typical STAP algorithms. (a) 1-D slice figure along Doppler dimension by using the $2\,\mathrm{DSW}_{+,3,3}$ algorithm. (b) 1-D slice figure along range dimension by using the $2\,\mathrm{DSW}_{+,3,3}$ algorithm. (c) 1-D slice figure along Doppler dimension by using the F\$A algorithm. (d) 1-D slice figure along range dimension by using the F\$A algorithm. (e) 1-D slice figure along Doppler dimension by using the order-2 EFA. (f) 1-D slice figure along range dimension by using the order-2 EFA. (g) 1-D slice figure along Doppler dimension by using the $\mathrm{JDL}_{3\times3}$ algorithm. (h) 1-D slice figure along range dimension by using the $\mathrm{JDL}_{3\times3}$ algorithm. (i) 1-D slice figure along Doppler dimension by using the STMB_{2+4} algorithm. (j) 1-D slice figure along range dimension by using the STMB_{2+4} algorithm. (k) 1-D slice figure along Doppler dimension by using the $\Sigma\Delta$-STAP algorithm. (l) 1-D slice figure along range dimension by using the $\Sigma\Delta$-STAP algorithm.

Table 12 Output SCNRs

Methods	Output SCNR
$2DSW_{+,3,3}$	21.35 dB
F\$A	24.22 dB
Order-2 EFA	20.89 dB
$JDL_{3\times3}$	20.87 dB
$STMB_{2+4}$	13.51 dB
$\Sigma\Delta$-STAP	13.84 dB

4) Influence of the Number of Training Samples

In this section, the influences of the number of training samples on the moving target detection performance by using different STAP algorithms are compared. Suppose that only 25 available range training samples around the moving target region in this real-measured radar data are applied. The clutter

suppression results after using $2DSW_{+,3,3}$, F\$A, order-2 EFA, $JDL_{3\times3}$, $STMB_{2+4}$, and $\Sigma\Delta$-STAP algorithms are shown in Fig. 24, where Figs. 24(a), (c), (e), (g), (i), (k) are the slice figures of the clutter suppression results of the 14th range gate (i.e., the range gate where the target is located at) along Doppler dimension, and Figs. 24(b), (d), (f), (h), (j), (l) are the slice figures of the clutter suppression results of the 74th Doppler gate (i.e., the Doppler gate where the target is located at) along range dimension. Table 13 lists the output SCNRs of this target by using these algorithms. From the figures, it is apparent that the target detection performance significantly degrades by using the order-2 EFA and F\$A algorithms due to the limited training samples. In contrast, the other algorithms can still effectively detect the moving target due to their low requirement of the training samples.
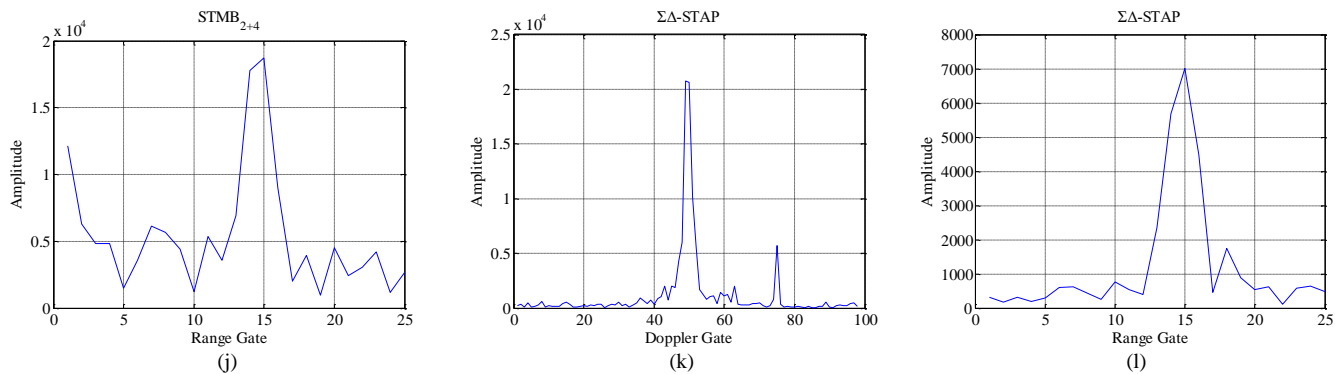

(a)

(b)

(c)

(d)

(e)

(f)

(g)

(h)

(i)
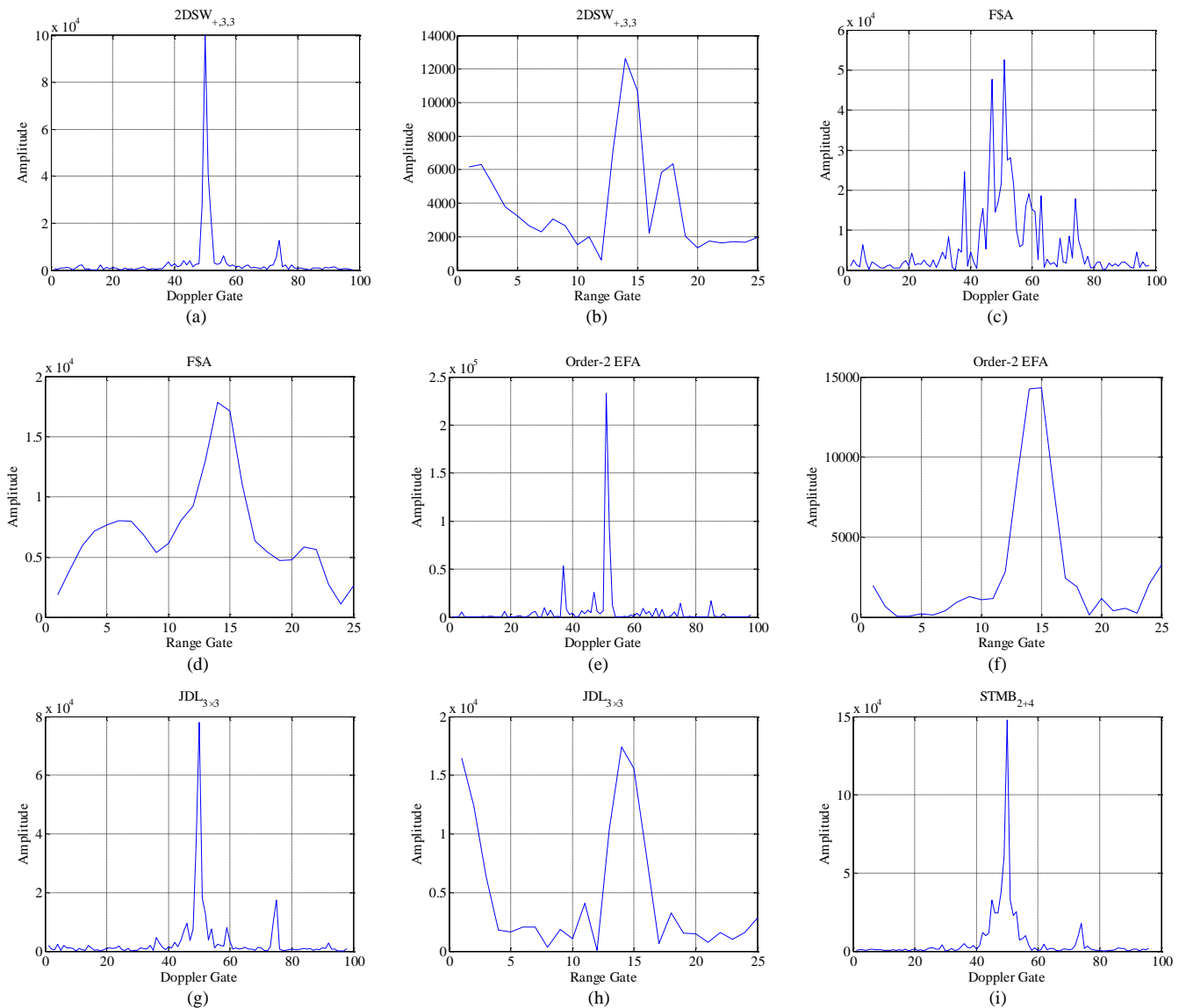
Fig. 24. Slice figures by using the proposed algorithm and other typical STAP algorithms. (a) Slice figure along Doppler dimension by using the $2\text{DSW}_{+,3,3}$ algorithm. (b) Slice figure along range dimension by using the $2\text{DSW}_{+,3,3}$ algorithm. (c) Slice figure along Doppler dimension by using the F$A algorithm. (d) Slice figure along range dimension by using the F$A algorithm. (e) Slice figure along Doppler dimension by using the order-2 EFA. (f) Slice figure along range dimension by using the order-2 EFA. (g) Slice figure along Doppler dimension by using the $\text{JDL}_{3\times3}$ algorithm. (h) Slice figure along range dimension by using the $\text{JDL}_{3\times3}$ algorithm. (i) Slice figure along Doppler dimension by using the STMB_{4+4} algorithm. (j) Slice figure along range dimension by using the STMB_{4+4} algorithm. (k) Slice figure along Doppler dimension by using the $\Sigma\Delta$-STAP algorithm. (l) Slice figure along range dimension by using the $\Sigma\Delta$-STAP algorithm.

Table 13 Output SCNRs

Methods	Output SCNR
$2\text{DSW}_{+,3,3}$	16.27 dB
F$A	9.86 dB
Order-2 EFA	9.60 dB
$\text{JDL}_{3\times3}$	15.23 dB
STMB_{2+4}	8.13 dB
$\Sigma\Delta$-STAP	15.31 dB

V. CONCLUSION

In this paper, a novel dimension-reduced STAP algorithm based on spatial-temporal 2-D sliding window is proposed, where multiple sets of spatial-temporal data are provided by using the 2-D window sliding, and then the jointly adaptive processing in the angle-Doppler domain is implemented. The simulated and real-measured radar data processing results verify the clutter suppression performance of the proposed algorithm. As a result, the proposed algorithm can considerably decrease the system computational complexity and the i.i.d. training sample demand, while achieving a good clutter suppression performance, indicating the application potential in practical engineering.

For a SEWR system, when the crab angle error caused by the Earth's rotation effect may not be ignored, the range ambiguities from the substellar point regions and the elevation main-lobe regions will not only enhance the clutter power, but also destroy the i.i.d. distribution property of clutter returns, dramatically worsening the clutter spatial filtering performance. How to alleviate the range-ambiguous clutter influences by using the waveform design and pulse phase coding techniques in a SEWR system will be under our future investigation.

APPENDIX

Usually, the STAP based methods utilize the target steering vector to calculate the clutter suppression weight vector, so as to realize the clutter suppression and the moving target CFAR detection. Therefore, the STAP methods will be influenced by the target steering vector mismatch. In this appendix, the influences of target steering vector mismatch on the proposed algorithm and other conventional STAP algorithms are analyzed according to the simulation data processing results (refer to Table 3 and Table 4 for simulated system parameters).

Suppose that the radial velocity of a moving target is 50 m/s, and the target spatial cone angle applied in STAP is set as 90 °. Fig. 25 shows the output SCNR curves by using $2\text{DSW}_{+,5,3}$, F$A, order-2 EFA, $\text{JDL}_{3\times3}$, STMB_{2+4}, $\Sigma\Delta$-STAP, and eigencanceler when the target actual spatial cone angle is set as 88 °~92 °. From the figure, it can be seen that all these STAP methods show similar SCNR downward tendency with the increase of spatial cone angle mismatch error, indicating that the influences of target steering vector mismatch on these methods are similar.
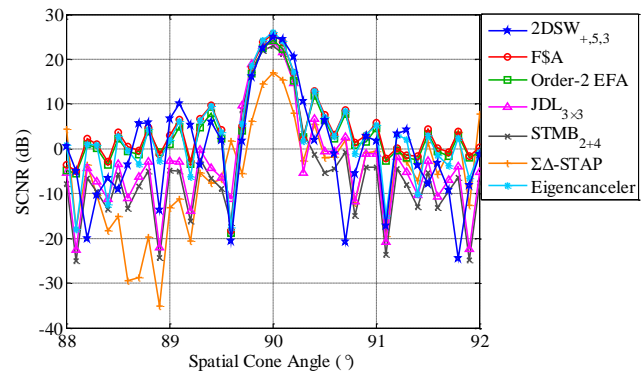

Fig. 25. Output SCNR curves by using the $2\text{DSW}_{+,5,3}$, F$A, order-2 EFA, $\text{JDL}_{3\times3}$, STMB_{2+4}, $\Sigma\Delta$-STAP, and eigencanceler with different spatial cone angles of a moving target.

To deal with the harmful influences of target steering vector mismatch, the angle search in the spatial angle domain can be applied to improve the moving target detection performance, which will inevitably increase the computational complexity. Usually, if the SCNR loss caused by steering vector mismatch is tolerable, the search step of spatial cone angle can be relatively large. In the case of target steering vector mismatch, how to further decrease the computational complexity of the proposed method will be under our next investigation.

REFERENCES

[1] M. I. Skolnik, *Radar Handbook*, 3rd ed. New York: McGraw-Hill, 2008.

[2] Y. Wang and Y. Peng, *Space-Time Adaptive Processing*. Beijing: Tsinghua University Press, 2000.

[3] S. V. Baumgartner and G. Krieger, "Fast GMTI algorithm for traffic monitoring based on a priori knowledge," *IEEE Trans. Geosci. Remote Sens.*, vol. 50, no. 11, pp. 4626-4641, Nov. 2012.

[4] A. Renga, M. D. Graziano, and A. Moccia, "Segmentation of marine SAR images by sublook analysis and application to sea traffic monitoring," *IEEE Trans. Geosci. Remote Sens.*, vol. 57, no. 3, pp. 1463-1477, Mar. 2019.

[5] J. Zhang, T. Ding, and L. Zhang, "Longtime coherent integration algorithm for high-speed maneuvering target detection using space-based bistatic radar," *IEEE Trans. Geosci. Remote Sens.*, Doi: 10.1109/TGRS.2020.3038199.

[6] M. V. Dragosevic, W. Burwash, and S. Chiu, "Detection and estimation with RADARSAT-2 moving-object detection experiment modes," *IEEE Trans. Geosci. Remote Sens.*, vol. 50, no. 9, pp. 3527-3543, Sept. 2012.

[7] B. Chen, *Modern Radar System Analysis and Design*. Xi'an: Xidian University Press, 2012.

[8] V. Gracheva and J. Ender, "Multichannel analysis and suppression of sea clutter for airborne microwave radar systems," *IEEE Trans. Geosci. Remote Sens.*, vol. 54, no. 4, pp. 2385-2399, Apr. 2016.

[9] V. Gracheva and D. C. Maori, "Multi-channel analysis of sea clutter for STAP applications," in *Proc. European Conference on Synthetic Aperture Radar*, Nurnberg, Germany, Apr. 2012, pp. 195-198.

[10] J. R. Guerci, *Space-Time Adaptive Processing for Radar*. London: Artech House, 2003.

[11] L. E. Brennan and I. S. Reed, "Theory of adaptive radar," *IEEE Trans. Aerosp. Electron. Syst.*, vol. 9, no. 2, pp. 237-252, Mar. 1973.

[12] X. Wang, E. Aboutanios, and M. G. Amin, "Reduced-rank STAP for slow-moving target detection by antenna-pulse selection," *IEEE Signal Process. Lett.*, vol. 22, no. 8, pp. 1156-1160, Aug. 2015.

[13] J. Xu, G. Liao, and H. C. So, "Space-time adaptive processing with vertical frequency diverse array for range-ambiguous clutter suppression," *IEEE Trans. Geosci. Remote Sens.*, vol. 54, no. 9, pp. 5352-5364, Sept. 2016.

[14] A. B. C. Silva, S. V. Baumgartner, and G. Krieger, "Training data selection and update strategies for airborne post-Doppler STAP," *IEEE Trans. Geosci. Remote Sens.*, vol. 57, no. 8, pp. 5626-5641, Aug. 2019.

[15] Z. Jiang, Y. He, G. Li, and X. Zhang, "Robust STAP detection based on volume cross-correlation function in heterogeneous environments," *IEEE Geosci. Remote Sens. Lett.*, Doi: 10.1109/LGRS. 2020. 3019580.

[16] W. Xie, K. Duan, and Y. Wang, "Space time adaptive processing technique for airborne radar: an overview of its development and prospects," *Journal of Radar*, vol. 6, no. 6, pp. 575-586, Dec. 2017.

[17] S. Han, C. Fan, and X. Huang, "A novel STAP based on spectrum-aided reduced-dimension clutter sparse recovery," *IEEE Geosci. Remote Sens. Lett.*, vol. 14, no. 2, pp. 213-217, Feb. 2017.

[18] R. Klemm, "Adaptive clutter suppression for airborne phased array radars," *IEE Proc. F*, vol. 130, no. 1, pp. 125-132, Feb. 1983.

[19] A. M. Haimovich, "The eigencanceler: a new space-time interference canceler," in *Proc. IEEE National Radar Conference*, Atlanta, USA, Mar. 1994, pp. 194-199.

[20] J. S. Goldstein and I. S. Reed, "Reduced-rank adaptive filtering," *IEEE Trans. Signal Process.*, vol. 45, no. 2, pp. 492-496, Feb. 1997.

[21] J. S. Goldstein and I. S. Reed, "Subspace selection for partially adaptive sensor array processing," *IEEE Trans. Aerosp. Electron. Syst.*, vol. 33, no. 2, pp. 539-544, Apr. 1997.

[22] J. S. Goldstein, I. S. Reed, and L. L. Scharf, "A multistage representation of the Wiener filter based on orthogonal projections," *IEEE Trans. Inf. Theory*, vol. 44, no. 7, pp. 2943-2959, Nov. 1998.

[23] Z. Zhang, W. Xie, W. Hu, and W. Yu, "Local degrees of freedom of airborne array radar clutter for STAP," *IEEE Geosci. Remote Sens. Lett.*, vol. 6, no. 1, pp. 97-101, Jan. 2009.

[24] W. F. Gabriel, "Adaptive digital processing investigation of DFT subbanding vs transversal filter canceler," Naval Research Laboratory, Technical Report AD-A171 894, July 1986.

[25] R. C. DiPietro, "Extended factored space-time processing for airborne radar systems," in *Proc. Asilomar Conference*, Pacific Grove, USA, Oct. 1992, pp. 425-430.

[26] L. E. Brennan, D. J. Piwinski, and F. M. Staudaher, "Comparison of space-time adaptive processing approaches using experimental airborne radar data," in *Proc. IEEE National Radar Conference*, Lynnfield, USA, Apr. 1993, pp. 176-181.

[27] R. D. Brown, M. C. Wicks, Y. Zhang, Q. Zhang, and H. Wang, "A space-time adaptive processing approach for improved performance and affordability," in *Proc. IEEE National Radar Conference*, Ann Arbor, USA, May 1996, pp. 321-326.

[28] R. Klemm, "Adaptive airborne MTI: an auxiliary channel approach," *IEE Proc. F*, vol. 134, no. 3, pp. 269-276, June 1987.

[29] H. Wang and L. Cai, "On adaptive spatial-temporal processing for airborne surveillance radar systems," *IEEE Trans. Aerosp. Electron. Syst.*, vol. 30, no. 3, pp. 660-670, July 1994.

[30] Y. Wang, Z. Wu, and Y. Peng, "A STAP approach for the non-homogeneous radar clutter environment," *Acta Electronica Sinica*, vol. 27, no. 9, pp. 55-58, Sept. 1999.

[31] Y. Wang, J. Chen, Z. Bao, and Y. Peng, "Robust space-time adaptive processing for airborne radar in nonhomogeneous clutter environments," *IEEE Trans. Aerosp. Electron. Syst.*, vol. 39, no. 1, pp. 70-81, Jan. 2003.

[32] S. U. Pillai, B. Himed, and K. Y. Li, "Effect of Earth's rotation and range foldover on space-based radar performance," *IEEE Trans. Aerosp. Electron. Syst.*, vol. 42, no. 3, pp. 917-932, July 2006.

[33] K. Y. Li and S. U. Pillai, "STAP for space based radar," Final Technical Report, Air Force Research Laboratory, AFRL-SN-RS-TR-2004-170, June 2004.

[34] M. E. Davis, B. Himed, and D. Zasada, "Design of large space radar for multimode surveillance," in *Proc. IEEE Radar Conference*, Huntsville, AL, May 2003, 106.

[35] P. Huang, Z. Zou, X.-G. Xia, G. Liao, and Z. Xin, "Multichannel sea clutter modeling for spaceborne early warning radar and clutter suppression performance analysis," *IEEE Trans. Geosci. Remote Sens.*, Doi: 10.1109/TGRS.2020.3039495.

[36] M. Villano, G. Krieger, and A. Moreira, "Staggered SAR: high-resolution wide-swath imaging by continuous PRI variation," *IEEE Trans. Geosci. Remote Sens.*, vol. 52, no. 7, pp. 4462-4479, July 2014.

[37] G. Krieger, N. Gebert, and A. Moreira, "Unambiguous SAR signal reconstruction from nonuniform displaced phase center sampling," *IEEE. Geosci. Remote Sens. Lett.*, vol. 1, no. 4, pp. 260-264, Oct. 2014.

[38] Z. Li, H. Wang, and Z. Bao, "Generation of wide-swath and high-resolution SAR images from multichannel small spaceborne SAR systems," *IEEE. Geosci. Remote Sens. Let.*, vol. 2, no. 1, pp. 82-86, Jan. 2005.

[39] N. A. Goodman, S. C. Lin, D. Rajakrishna, and J. M. Stiles, "Processing of multiple-receiver spaceborne arrays for wide-area SAR," *IEEE Trans. Geosci Remote Sens.*, vol. 40, no. 4, pp. 841-852, Apr. 2002.

[40] J. Jao, "Theory of synthetic aperture radar imaging of a moving target," *IEEE Trans. Geosci. Remote Sens.*, vol. 39, no. 9, pp. 1984-1992, Sept. 2001.

[41] Y. Zhang, A. Hajjari, K. Kim, and B. Himed, "A dual-threshold ATI-SAR approach for detecting slow moving targets," in *Proc. IEEE Radar Conference*, Arlington, VA, USA, May 2005, pp. 295-299.

[42] D. Cerutti-Maori, J. Klare, A. R. Brenner, and J. G. H. Ender, "Wide area traffic monitoring with the SAR/GMTI system PAMIR," *IEEE Trans. Geosci. Remote Sens.*, vol. 46, no. 10, pp. 3019-3030, Oct. 2008.

[43] C. H. Gierull, I. Sikaneta, and D. Cerutti-Maori, "Two-step detector for RADARSAT-2's experimental GMTI mode," *IEEE Trans. Geosci. Remote Sens.*, vol. 51, no. 1, pp. 436-454, Jan. 2013.

[44] P. Huang, G. Liao, Z. Yang, X.-G. Xia, J.-T. Ma, and X. Zhang, "A fast SAR imaging method for ground moving target using a second-order WVD transform," *IEEE Trans. Geosci. Remote Sens.*, vol. 54, no. 4, pp. 1940-1956, Apr. 2016.

[45] L. Ding, F. Geng, and J. Chen, *Radar Principles*, 5th ed. Beijing: Publishing House of Electronics Industry, 2014.

[46] P. A. Rosen and M. E. Davis, "A joint space-borne radar technology demonstration mission for NASA and the air force," in *Proc. IEEE Aerospace Conference*, Big Sky, USA, Mar. 2003, pp. 437-444.

[47] P. Zhao, Z. Wu, Y. Zhang, Y. Zhang, and Z. Yin, "The theoretical and experimental study on backscattering from arable land," in *Proc. International Symposium on Antennas Propagation and EM Theory*, Xi'an, China, Oct. 2012, pp. 845-848.

[48] W. L. Melvin, M. C. Wicks, and R. D. Brown, "Assessment of multichannel airborne radar measurements for analysis and design of space-time processing architectures and algorithm," in *Proc. IEEE National Radar Conference*, May 1996, pp. 130-135.

[49] W. L. Melvin and M. C. Wicks, "Improving practical space-time adaptive radar," in *Proc. IEEE National Radar Conference*, May 1997, pp. 48-53.

This article has been accepted for publication in a future issue of this journal, but has not been fully edited. Content may change prior to final publication. Citation information: DOI 10.1109/TGRS.2022.3144668, IEEE Transactions on Geoscience and Remote Sensing

Accepted Manuscript
Version of record at: : https://doi.org/10.1109/TGRS.2022.314

21

[50] G. N. Schoenig, M. L. Picciolog, and L. Mili, "Improved detection of strong nonhomogeneities for STAP via projection statics," in *Proc. IEEE International Radar Conference*, May 2005, pp. 720-725.

Penghui Huang (M'17) was born in Jiangxi, China. He received the B.S. and PH.D. degrees in electrical engineering from Xidian University, Xi'an, China, in 2012 and 2017, respectively.

He joined in the School of Electronic Information and Electrical Engineering, Shanghai Jiao Tong University, Shanghai, China, in 2017. He was an Assistant Professor from 2017 to 2021, and he is currently an Associate Professor and a Ph.D adviser. His research interests include space-borne early warning radar system design, space-time adaptive processing (STAP), multi-channel sea clutter modeling, simulation, space-time property analysis, and robust suppression, distributed space-borne wide-area surveillance radar signal processing with ground moving target indication (GMTI) as well as air moving target indication (AMTI), space-borne HRWS-SAR imaging, ISAR imaging, and weak target detection and tracking. He was the recipient of the Prize for Excellent Ph.D. degree dissertation of the Chinese Institute of Electronics education in 2017, and also the recipient of the Prize for Excellent Ph.D. degree dissertation of the Shaanxi Province in 2019.

Dr. Huang is a Reviewer of the IEEE Transactions on Geoscience and remote sensing, the IEEE Transactions on Aerospace and Electronic Systems, the IEEE Transactions on Signal Processing, the IEEE Journal of Selected Topics in Applied Earth Observations and Remote Sensing, the IEEE Sensor Journals, the IEEE Geoscience and Remote Sensing Letters, etc.

Zihao Zou was born in Zhejiang, China. He is pursuing the Ph.D. degree with the School of Electronic Information and Electrical Engineering, Shanghai Jiao Tong University, Shanghai, China.

His research interests include space-time adaptive processing (STAP), sea clutter modeling and simulation, and maritime target detection.

Xiang-Gen Xia (M'97, S'00, F'09) received his B.S. degree in mathematics from Nanjing Normal University, Nanjing, China, and his M.S. degree in mathematics from Nankai University, Tianjin, China, and his Ph.D. degree in electrical engineering from the University of Southern California, Los Angeles, in 1983, 1986, and 1992, respectively.

He was a Senior/Research Staff Member at Hughes Research Laboratories, Malibu, California, during 1995-1996. In September 1996, he joined the Department of Electrical and Computer Engineering, University of Delaware, Newark, Delaware, where he is the Charles Black Evans Professor. His current research interests include space-time coding, MIMO and OFDM systems, digital signal processing, and SAR and ISAR imaging. Dr. Xia is the author of the book Modulated Coding for Intersymbol Interference Channels (New York, Marcel Dekker, 2000).

Dr. Xia received the National Science Foundation (NSF) Faculty Early Career Development (CAREER) Program Award in 1997, the Office of Naval Research (ONR) Young Investigator Award in 1998, and the Outstanding Overseas Young Investigator Award from the National Nature Science Foundation of China in 2001. He received the 2019 Information Theory Outstanding Overseas Chinese Scientist Award, The Information Theory Society of Chinese Institute of Electronics. Dr. Xia has served as an Associate Editor for numerous international journals including IEEE Transactions on Signal Processing, IEEE Transactions on Wireless Communications, IEEE Transactions on Mobile Computing, and IEEE Transactions on Vehicular Technology. Dr. Xia is Technical Program Chair of the Signal Processing Symp., Globecom 2007 in Washington D.C. and the General Co-Chair of ICASSP 2005 in Philadelphia.

Xingzhao Liu (M'04) received the B.S. and M.S. degrees from Harbin Institute of Technology, Harbin, China, in 1984 and 1992, respectively, and the Ph.D. degree from the University of Tokushima, Tokushima, Japan, in 1995, all in electrical engineering.

He was an Assistant Professor, an Associate Professor, and a Professor with Harbin Institute of Technology, from 1984 to 1998. Since 1998, he has been a Professor with Shanghai Jiao Tong University, Shanghai, China. His research interests include high-frequency radar and synthetic aperture radar signal processing.

Guisheng Liao (M'96~SM'16) was born in Guiling, China. He received the B.S. degree from Guangxi University, Guangxi, China, and the M.S. and Ph.D. degrees from Xidian University, Xi'an, China, in 1985, 1990, and 1992, respectively.

He is currently a Professor with Xidian University, where he is also Dean of School of Electronic Engineering. He has been a Senior Visiting Scholar in the Chinese University of Hong Kong, Hong Kong. His research interests include synthetic aperture radar (SAR), space–time adaptive processing, SAR ground moving target indication, and distributed small satellite SAR system design. Prof. Liao is a member of the National Outstanding Person and the Cheung Kong Scholars in China.